

AD-A032 186

ILLINOIS UNIV AT URBANA-CHAMPAIGN COORDINATED SCIENCE LAB F/8 9/2
RESEARCH ON DISPLAY DATA INTEGRATION IN SYSTEMS WHICH USE FLAT --ETC(U)
FEB 75 R L JOHNSON, H G SLOTTOW, L F WEBER N00014-67-A-0305-0021

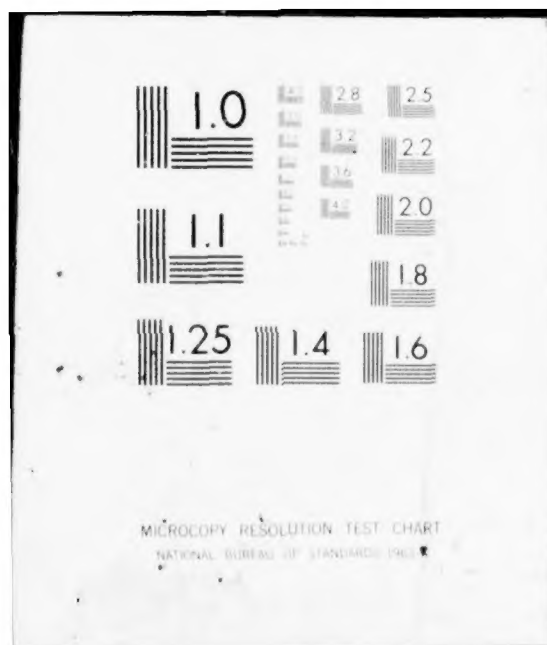
UNCLASSIFIED

NL

1 OF 2

AD
A032186





ADA032186

FEBRUARY, 1975

CSL COORDINATED SCIENCE LABORATORY

Del 14730

**RESEARCH ON DISPLAY DATA
INTEGRATION IN SYSTEMS
WHICH USE FLAT AC PLASMA PANEL
DISPLAYS WITH INHERENT MEMORY**

R.L. JOHNSON (PRINCIPAL INVESTIGATOR)
H.G. SLOTTOW
L.F. WEBER
A.B. WHITE

OFFICE OF NAVAL RESEARCH
CONTRACT N00014-67-A-0305-0021
ONR TASK: NR 215-197
MODIFICATION: 03

FINAL TECHNICAL REPORT

DDC
RECEIVED
NOV 18 1975
RECEIVED

APPROVED FOR PUBLIC RELEASE. DISTRIBUTION UNLIMITED.

UNIVERSITY OF ILLINOIS - URBANA, ILLINOIS

FOREWORD

This report contains results of a research program designed to investigate techniques for reducing interface electronics and improving performance and reliability in display systems which use AC plasma display panel devices and to study the effects of these display systems on computer-based instrumentation systems. The program was under the direction of R. L. Johnson, Associate Research Professor at the University of Illinois Coordinated Science Laboratory, Urbana, Illinois under Contract N00014-67-A-0305-0021, Task NR 215-197 for the Office of Naval Research, Arlington, Virginia 22217. The Technical Program Monitor was initially LCDR H. B. Lyons, then LCDR R. Hudson, and finally Mr. G. Flohil. Portions of the work described in this report were performed in cooperation with the University of Illinois Aviation Research Laboratory under the direction of Dr. S. Roscoe and the University of Illinois Computer-based Education Research Laboratory under the direction of Dr. D. L. Bitzer. The work described here was performed during the period from 1 January 1974 to 31 December 1974.

The author wishes to acknowledge and thank Mr. L. Weber, Mr. A. White, Ms. M. Stone, Dr. H. G. Slottow, Mr. M. Marentic, Mr. W. Coates, Mr. G. Weikart, Mr. J. Roberts, Mr. F. Ebeling, Mr. R. Rader, and Mr. D. Sleator for their significant technical contributions in the completion of the program tasks.

ACCESSION for	
NTIS	White Section <input checked="" type="checkbox"/>
DDC	Buff Section <input type="checkbox"/>
UNANNOUNCED	<input type="checkbox"/>
JUSTIFICATION	
BY	
DISTRIBUTION/AVAILABILITY CODES	
DISC.	AVAIL. DISC. or SPECIAL
A	

DDC
RECEIVED
NOV 18 1976
A

TABLE OF CONTENTS

	Page
I. INTRODUCTION.....	1
II. PHYSICS OF AC DISCHARGES.....	4
2.1 Introduction.....	4
2.2 Computer Model.....	4
2.2.1 Method of Calculation.....	4
2.2.2 Results of Calculations.....	10
2.3 Capacitance Measurements.....	15
2.4 Microwave Measurements.....	24
2.5 Optical Interferometry.....	27
2.5.1 An Accurate Interferometer.....	28
2.5.2 Interferometric Measurements on Plasma Display Cells.....	41
2.5.2.1 Atom Density Measurements.....	47
2.5.2.2 Electron Density Measurements.....	56
2.5.3 Glass Surface Properties.....	60
III. INTERNAL LOGIC.....	63
3.1 Introduction.....	63
3.2 Panel Decoding.....	63
3.3 A New Technique for Writing.....	67
IV. SPATIAL GRAY SCALE.....	70
4.1 Introduction.....	70
4.2 Dot Density Methods.....	70
4.3 Hardware Implementation.....	73
4.4 Data Compression.....	76
V. SYSTEMS RESEARCH.....	84
5.1 Graphic Display Terminal/Host System Architecture Studies...	84
5.2 An Experimental Intelligent Terminal Design.....	89
5.2.1 Hardware Architecture.....	90
5.2.2 Terminal Software.....	93
5.3 Specific Studies Relating to the PLATO IV System.....	96
5.4 Conclusions of System Studies.....	99
REFERENCES.....	100

List of Figures

Figure	Caption
2.1	Applied voltage and discharge current as a function of time.
2.2	Log plot of electron charge density as a function of space and time.
2.3	Electric field as a function of space and time.
2.4	Plasma cell capacitance as a function of time due to the growth and decay of the plasma region.
2.5	Resonance technique for measuring plasma cell capacitance.
2.6	RF envelope of 19 MHz signal in upper trace.
2.7	RF envelope as in Figure 2.6 but with rf oscillator slightly detuned.
2.8	Quarter wave stub technique for measuring plasma cell capacitance.
2.9	RF envelope of 57 MHz signal in upper trace.
2.10	Microwave strip line plasma cell.
2.11	Microwave transmission data in lower trace and low frequency capacitance envelope in upper trace, for strip line cell shown in Figure 2.10.
2.12	Jamin interferometer arrangement.
2.13	Interferometry system for measuring very small index of refraction changes in plasma cells.
2.14	Voltage, in upper trace, applied to Kerr cell to obtain the optical phase shift measured in lower trace by interferometer of Figure 2.13.
2.15	Basic geometry of plasma cell electrodes used in interferometry experiments.
2.16	Typical phase change results obtained with an Argon ion laser.
2.17	Multiple exposure photograph showing the index of refraction at 5 points along the discharge gap, as a function of time.

Figure	Caption
2.18	Optical phase changes for two discharges in cell with 250 torr Xe.
2.19	Phase changes in Xe filled cell showing slow density changes due to slow gas temperature changes.
2.20	Same conditions as in Figure 2.19 but with time scale 200 μ s/div.
2.21	Same conditions as in Figures 2.19 and 2.20 but with time scale 50 μ s/div.
2.22	Avalanche currents in a glass cell having an electrode separation of 2.5 cm and filled with 5 torr Ne and 0.25 torr N ₂ .
3.1	Electrode arrangement for four-input internal logic system.
4.1	The ordered dither matrix.
4.2	Block diagram of drive circuitry.
4.3	A system to generate ordered dither for the plasma panel interface.
4.4	An example of an image generated on a 512-60 Digivue using the ordered dither system.
4.5	Compression ratios for the 4 sample files using the N x M pattern codes and the 4-bit linear pattern code.
4.6	The number of different patterns found in each sample file.
5.1	Architecture of a large computer-based information system.
5.2	Architectures for future computer-based information systems.
5.3	Hardware arrangement used in experimental intelligent terminal.
5.4	Terminal software architecture.

ABSTRACT

A program of research to explore new display device techniques and digital system architecture concepts which can be used to realize highly reliable, low cost interactive graphic display systems has been completed at the University of Illinois Coordinated Science Laboratory. The techniques and concepts which were studied are generally applicable to future large scale computer-based information systems such as those used in ground based operations as well as in specialized computer-based information systems such as those used in aircraft, submarine, and shipboard instrumentation systems. The program during the last contract period was divided into four major areas.

A major part of the program has been the development of new techniques for the study of the discharge processes in the plasma display device, and the development of a more precise understanding of these processes. A second area of investigation, based in part on the first, is the search for new methods of enhancing the logical capability of the plasma display device. A third area is an investigation of spatial gray scale. And finally a study has been made of the architecture of computer-based information processing systems which emphasize direct interaction of users through graphical displays.

This report describes the significant results in each of the four areas of work.

I. INTRODUCTION

The diversity of topics discussed in this report reflects an interesting aspect of the present period in plasma display development. On the one hand the availability of commercial devices with more than 250,000 bistable addressable elements makes possible experimental research in the architecture of computer-based information processing systems, particularly systems that emphasize user interaction, and that require graphic displays. On the other hand the basic discharge processes on which the operation of the device ultimately depends are just beginning to be understood in detail. There is thus both need and opportunity to do fundamental device research. Both areas of investigation are discussed in this report.

One reason that more fundamental device research has not been done is that traditional computer simulation of the complicated electrical discharge processes has been expensive. However, by running computer programs as part of the background processing in the PLATO computer-based education environment it has been possible to simulate the discharge processes with a detail not attempted before. Another deterrent to basic research has been that experimental techniques usually appropriate for gas discharge studies are difficult in the environment of the plasma display cell for which a characteristic dimension is about 30 microns. New techniques which include electromagnetic interactions from radio to optical frequencies have been devised to obtain data from the discharge. One result of this work is the development of a new interferometric technique for measuring phase shifts on smaller than 10^{-5} Angstroms. This work and its

application to plasma cell measurements are described in detail in the following section along with results of both computer calculation and other experimental studies.

An application of the basic studies is the enhancement of logic through control of the gas discharge processes. While the preliminary results are mostly conceptual, the techniques seem to be sound, and the importance of simplifying addressing of plasma displays warrants discussion here.

The importance of finding ways of encoding images for transmission in information processing systems has led to research on algorithms for providing gray scale through dot density control. In particular a simple, inexpensive realization has been found and implemented for a new algorithm developed at Bell Laboratories. Studies on data compression techniques for this system are also discussed.

Finally, systems studies have provided results in two areas. First, results from the terminal system/host system architecture studies have provided definite guidelines as to how logical processing power and memory should be allocated in computer-based information and instrumentation systems which consist of a host system and remote flat panel graphics terminals which are connected via low bandwidth communication lines. These results are applicable to both ground based information systems as well as aircraft, submarine, and shipboard instrumentation and information systems.

Second, specific terminal architecture considerations related to the results of the first area have emerged. Microprocessor based display terminals and display terminals which used considerable local processing

power and memory located near or on the display have undergone extensive study. Specific recommendations for future terminal structures have been made.

Each of the research areas discussed in this report is in an early phase of development. Each is important to the development of plasma display technology, and we expect that each will receive increasing emphasis over the next few years.

II. PHYSICS OF AC DISCHARGES

2.1 Introduction

This section describes research that is aimed at a complete understanding of the many gas discharge processes found in the AC plasma display panel. The program includes computer modeling and development of measurement techniques needed to confirm the model. The major results show the existence of a large plasma in the gas volume for tens of microseconds after the discharge. Neutral atom densities can be measured as a function of space and time, and be used to indicate the regions of intense discharge activity. Also the experiments show that the ion secondary effects mechanism predominates over the photon mechanism for soda glass cathodes.

2.2 Computer Model

2.2.1 Method of Calculation

Recently, a number of papers have appeared that model the plasma panel discharge process. [1,2,3,4] All use finite difference techniques with varying degrees of complexity. Veron and Wang [1] used the most rigorous method of calculation which was originally developed by Ward [5,6,7,8,9]. With this very time consuming technique, the calculation of the processes occurring for 1 microsecond in a plasma panel can take about 1 hour of CPU time on a large scale computer. Because of the obvious cost factors, Veron and Wang did not run very much data. Lay et al. [3], circumvented the CPU time problem by neglecting the field distortion in the discharge gap caused by the large densities of ions and electrons. As

will be shown later in this paper, this is a very poor approximation. Lanza [4] has developed a very clever technique for reducing the CPU time required without neglecting field distortion. Although Lanza presents excellent agreement between experimental and calculated currents, the calculations and measurements described below tend to show significant errors.

The basic calculational technique uses a first order finite difference technique to solve the following equations in one dimension. The basic three equations to be solved are: the electron continuity equation

$$\frac{\partial n_e}{\partial t} = \alpha n_e V_e - \frac{\partial}{\partial x} (n_e V_e) \quad (1)$$

which qualitatively says the rate of change of electron density at a point in space ($\frac{\partial n_e}{\partial t}$) is equal to the rate of electron generation in the gap ($\alpha n_e V_e$) plus the rate of the electrons coming in minus the rate of electrons going out of that point ($-\frac{\partial}{\partial x}(n_e V_e)$). Similarly the ion continuity equation is

$$\frac{\partial n_i}{\partial t} = \alpha n_e V_e + \frac{\partial}{\partial x} (n_i V_i) \quad (2)$$

where n_e is the electron number density, n_i is the ion number density, V_e is the electron velocity, V_i is the ion velocity, α is the Townsend coefficient that describes the number of electrons freed by the avalanche process per unit length, x is space, and t is time. The variables n_e , n_i , V_e , V_i , and α are all functions of both x and t . The variables V_e , V_i ,

and α are characteristic of the gas and are directly dependent on the value of the electric field $E(x,t)$ which must be found from Poisson's equation:

$$\frac{\partial E}{\partial x} = \frac{q}{E_0} (n_1 - n_e) \quad (3)$$

where q is the charge of the electron and E_0 is the dielectric constant of free space.

From the above three equations and knowledge of the functional relationship of V_e , V_1 , and α on E , one can find the desired solution which is n_e and n_1 for all values of space and time if the necessary boundary conditions and initial conditions are specified. In a gas discharge a number of physical effects can occur at the cathode that will define the cathode boundary conditions. If we define an electron current density $j_e(x,t) = n_e(x,t) \cdot V_e(x,t)$, then this cathode boundary condition is specified by the electron current from the cathode

$$j_e(0,t) = j_0 + \gamma_1 j_1(0,t) + \frac{\gamma_p}{d} \int_0^d \sigma(x,t) j_e(x,t) dx \quad (4)$$

where j_0 is a very small constant current emitted from the cathode to get the discharge process started, γ_1 and γ_p are the Townsend coefficients for electrons emitted from the cathode due to ion bombardment and photon bombardment respectively, d is the distance between the cathode and the anode and σ is a function of x and t that defines the number of photons per unit distance created in an avalanche by an electron. The value of $\sigma(x,t)$ is determined from $E(x,t)$ in much the same manner as is $\alpha(x,t)$. γ_1 , γ_p and d are constants that characterize the discharge.

Since ions are not allowed to be emitted from the cathode

$$j_i(0,t) = 0 \quad (5)$$

Similarly nothing is allowed to be emitted by the anode, thus

$$j_e(d,t) = 0 \quad (6)$$

and

$$j_i(d,t) = 0 \quad (7)$$

Equations (4,5,6,7) define the boundary conditions that determine n_e and n_i . To determine $E(x,t)$, we must use Kirkhoff's voltage law and sum around the loop that includes the plasma display cell and the applied voltage source (sustainer). The loop equation is

$$V_s = E_c l + E_a l + E_o d + \frac{\lambda p}{\epsilon_o} \int_0^d \int_0^{x'} (n_e - n_i) dx dx' \quad (8)$$

where E_c and E_a are the fields in the dielectric layers at the cathode and the anode, l is the thickness of these dielectric layers, and E_o is the field in the gas volume at $x=0$. To find the values of the fields in the dielectric, E_c and E_a , one must know the value of the charges Q_o and Q_d at the dielectric gas interfaces. From the standard electric field boundary conditions one gets

$$\epsilon_r E_c - E_o = \frac{Q_o}{\epsilon_o} \quad (9)$$

and

$$E_d - \epsilon_r E_a = \frac{Q_d}{\epsilon_o}$$

where ϵ_r is the relative dielectric constant of the dielectric layers and E_d is the electric field in the gas volume at $x=d$.

The charges Q_o and Q_d are obtained by integrating all currents flowing into and out of the cathode and anode.

For initial conditions one must specify $n_e(x,0)$, $n_i(x,0)$, $Q_o(t=0)$, and $Q_d(t=0)$. The sustain voltage V_g is the desired function of time.

The gas parameters used those given by Ward [5]. The dependence of α , V_e , and V_i on the E field is

$$\alpha = pA \exp[-B(p/E)^{1/2}] \quad (11)$$

where p is the gas pressure and A and B are constants characteristic of the gas.

$$V_e = \frac{\mu_- E}{p} \quad (12)$$

where μ_- is the electron mobility.

$$V_i = \frac{\mu_+ E}{p} \left(1 - \frac{CE}{p}\right), \quad E/p \leq w_1 \quad (13a)$$

$$V_i = \frac{k_+ E^{1/2}}{p^{1/2}} \left(1 - DE^{-3/2} p^{3/2}\right), \quad E/p > w_1 \quad (13b)$$

where μ_+ , k_+ , C , D , and w_1 are constants characteristic of the gas. Ward [5] gives values of these constants for various gases. In the examples used here, pure Ne was used and has the following constants

$$A = 8.2 \text{ cm}^{-1} \text{ torr}^{-1}$$

$$B = 17.0 \text{ volt}^{1/2} \text{ cm}^{-1/2} \text{ torr}^{-1/2}$$

$$C = 6 \times 10^{-3} \text{ torr cm volt}^{-1}$$

$$\begin{aligned}
 D &= 41.98 \text{ volt}^{3/2} \text{ cm}^{-3/2} \text{ torr}^{-3/2} \\
 \mu_- &= 10^6 \text{ cm}^2 \text{ torr volt}^{-1} \text{ sec}^{-1} \\
 \mu_+ &= 2.9 \times 10^3 \text{ cm}^2 \text{ torr volt}^{-1} \text{ sec}^{-1} \\
 k_+ &= 1.7 \times 10^4 \text{ cm}^{3/2} \text{ torr}^{1/2} \text{ volt}^{-1/2} \text{ sec}^{-1}
 \end{aligned}$$

The calculational procedure follows. In finite difference calculations, each iteration produces a solution advanced by a time increment Δt . This value is chosen from a convergence criteria [9]:

$$\frac{\Delta t}{\Delta x} < \max |v_e(x, t)|_x \quad (14)$$

where Δx is the distance between mesh points. This relation simply states that one must calculate the next iteration before the fastest electrons have time to get from one mesh point to the next. Failure to obey (14) causes the calculation to blow up. For 30 mesh points across the discharge gap and for typical plasma panel conditions, Δt is about 10 ps. Thus for 1 μ s of plasma panel data, the following sequence is iterated 10^5 times.

1. Given the initial values of Q_0 , Q_d , $V_g(t)$, $n_e(x, t)$, $n_i(x, t)$, calculate for all x $E(x, t)$ from (3), (8), (9), and (10).
2. Calculate $V_e(x, t) = \frac{\mu_-}{p} E(x, t)$ for all x .
3. Calculate for all x $j_e(x, t) = V_e(x, t) n_e(x, t)$.
4. Calculate $V_i(x, t)$ from (13) for all x .
5. Calculate $j_i(x, t) = V_i(x, t) n_i(x, t)$ for all x .
6. Determine $\Delta t = \frac{0.9 \cdot \Delta x}{\max |V_e(x, t)|_x}$.
7. Calculate $t = t + \Delta t$.
8. Calculate $n_e(x, t)$ from a difference equation derived from (1) with the aid of (4) for all x .

9. Calculate $n_1(x,t)$ from a difference equation derived from (2).
10. Calculate $Q_o = Q_o + \Delta t \cdot j_i(0,t)$
 $Q_x = Q_x - \Delta t \cdot j_e(d,t)$
11. Return to step 1.

2.2.2 Results of Calculations

The data presented here are a typical sample from more than 1000 hours of CPU computations performed over the past 2 years. These data were computed in a background mode on the CDC Cyber 73 (6500) used by the PLATO terminals having a 512 x 512 AC plasma panel. The first 3 figures presented here are taken directly from a PLATO terminal. The ability to rapidly observe and manipulate the various desired functions gives the researcher a very useful qualitative understanding of the processes that has led to a number of creative advances.

Figure 2.1 shows the applied voltage and discharge current pulse for a typical one dimensional plasma display cell. This is qualitatively similar to all previously presented data. Figure 2.2 shows the electron charge density as a function of the space between the cathode and the anode. This shows the early exponential growth on the lower right hand side, the build up to a very large electron density that fills the entire gap except for the cathode region, and then the slow decay of the large electron density toward the anode. Each complete line shown in Figure 2.2 is composed of 14 straight line segments that connect 15 data points for 15 positions in the gap. Thus the decay of electrons is not accurately represented in Figure 2.2 due to undersampling. The peak of the discharge current shown

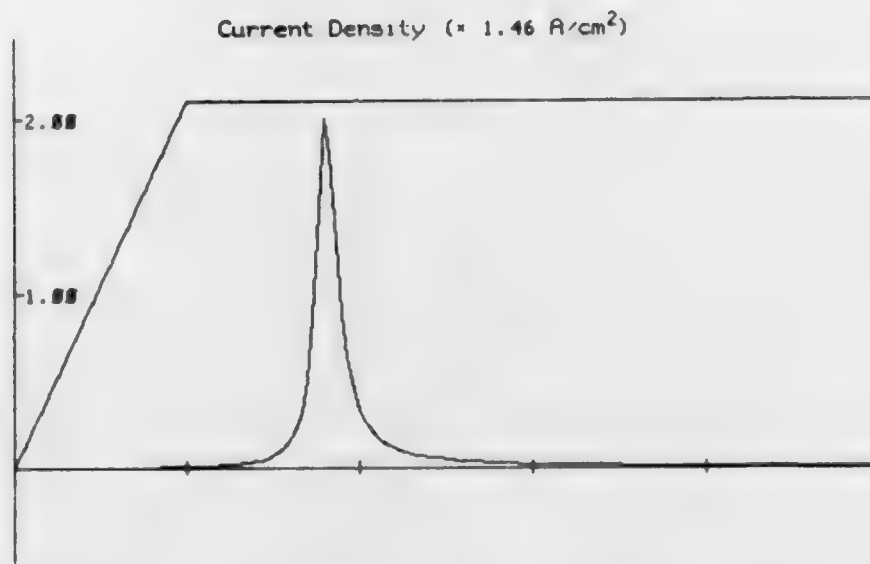


Figure 2.1. Applied voltage and discharge current as a function of time. Vertical scale is 100 volts/division and 1.46 Amp/cm^2 per division. Horizontal scale: 100 ns per division.

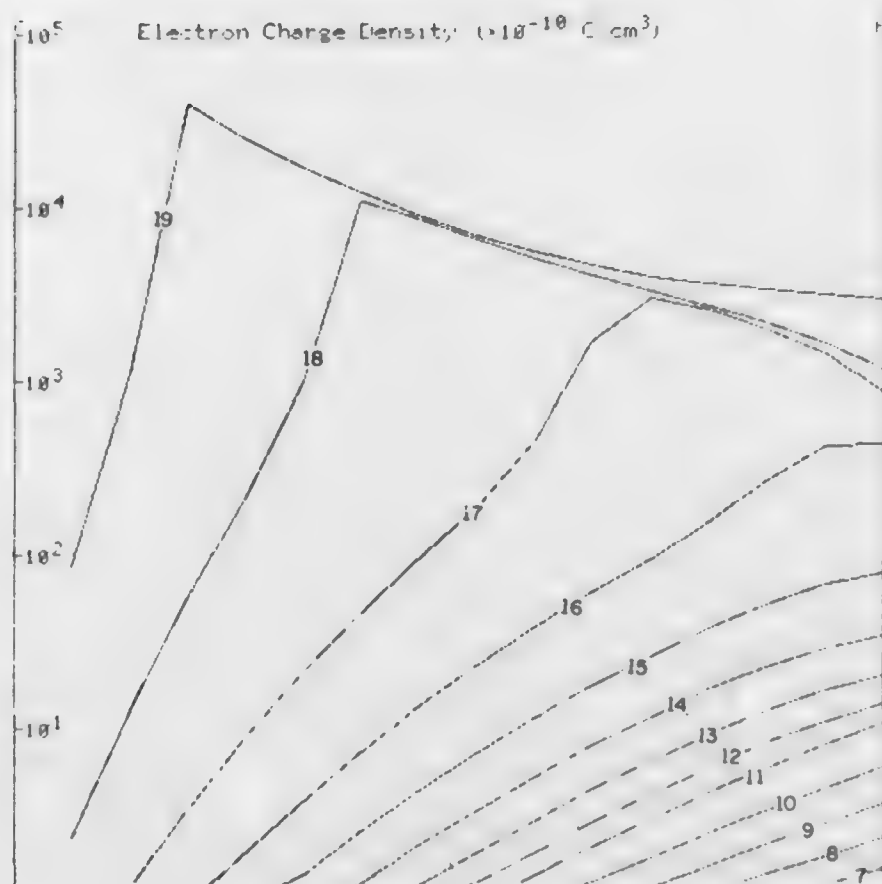


Figure 2.2. Log plot of electron charge density as a function of space and time. The cathode is on left and the anode on right. A time increment of 10 ns separates each curve. The origin of the vertical axis is 10^{-10} coulombs/cm³.

in Figure 2.1 closely corresponds to the curve showing the maximum total electron density in Figure 2.2.

The major difference between previous calculations and those presented here is the very large and slowly decaying electron density shown in Figure 2.2. This is typical of all data computed here using Ward's finite difference technique. If one looks at the corresponding ion density distribution, one finds it almost identical to the electron density after the peak of the discharge current. This is in fact a plasma as defined by the strict sense that the Debye length is much shorter than the cell dimensions. The electron and ion densities are so great that they cancel out most of the electric field on the anode side of the gap. With little electric field, the electrons and ions can move only by the slow diffusion process or can slowly recombine and are thus effectively trapped. Typically this plasma region exists for a number of microseconds after the discharge. It is not uncommon for the plasma to still exist when the sustain waveform falls 5 or 10 microseconds after the discharge. Thus with certain sustain waveforms, the existence of the plasma from the previous discharge can be a very important initial boundary condition.

The electric field as a function of gap spacing is shown in Figure 2.3. The field is initially equal for every point along the gap and increases as the sustain waveform rises. When the discharge occurs, the field at the anode decreases due to the growth of the plasma, and thus makes the field at the cathode very large. It is not uncommon to see cathode fields larger than 10^5 volts/cm. It is interesting to note that field emission has been observed for these fields intensities and

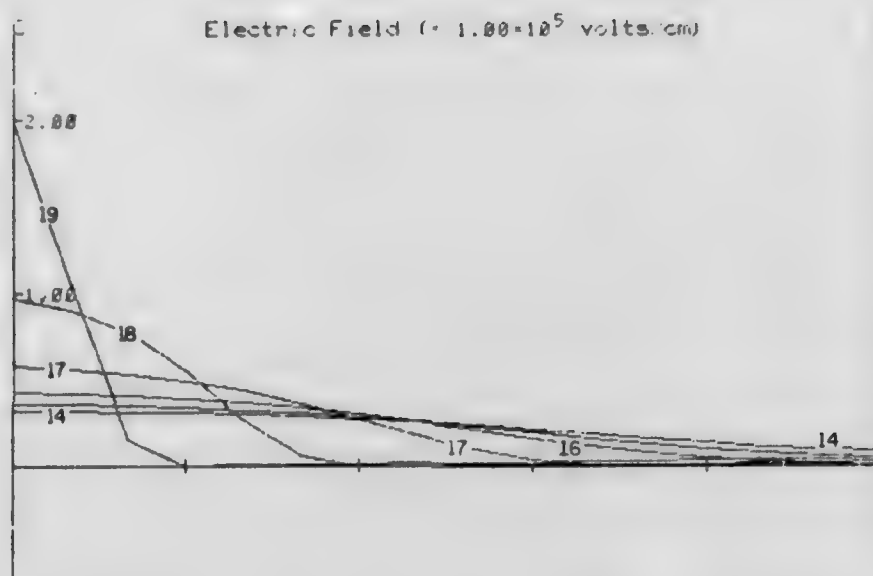


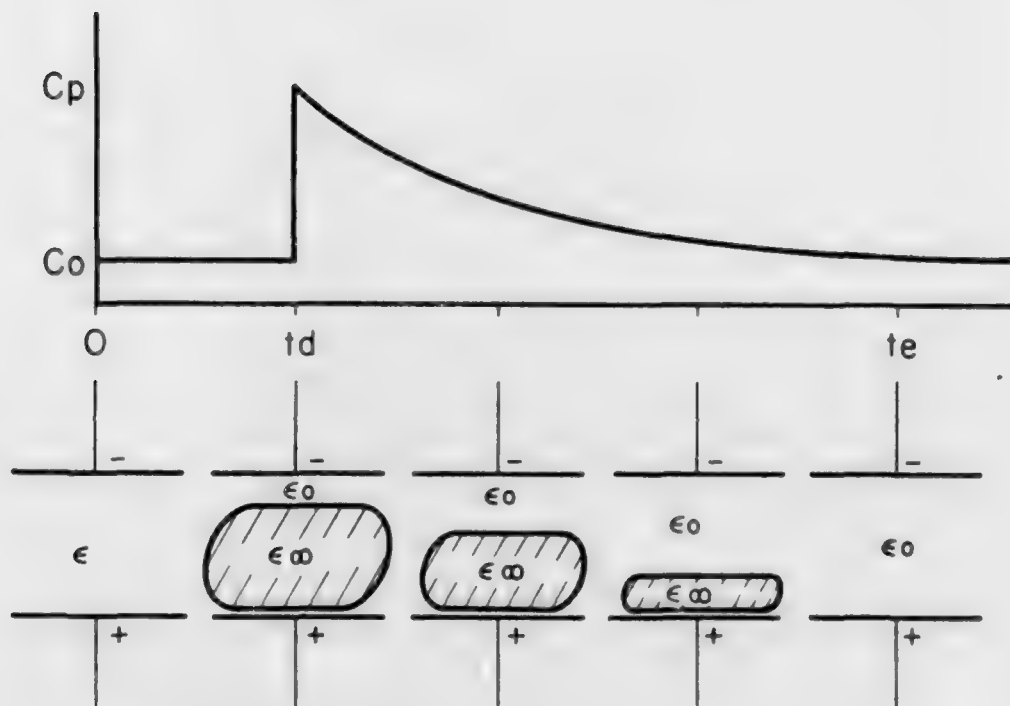
Figure 2.3. Electric field as a function of space and time. As for Figure 2.2 the time increment is 10 ns and the cathode is on the left. The vertical scale factor is 10^5 volts/cm.

thus might be an important cathode emission process at the peak of the discharge. Note also that most of the discharge activity or light output occurs near the cathode which is consistent with Anderson's measurements [10]. Also the field in the plasma region is near zero.

2.3 Capacitance Measurements

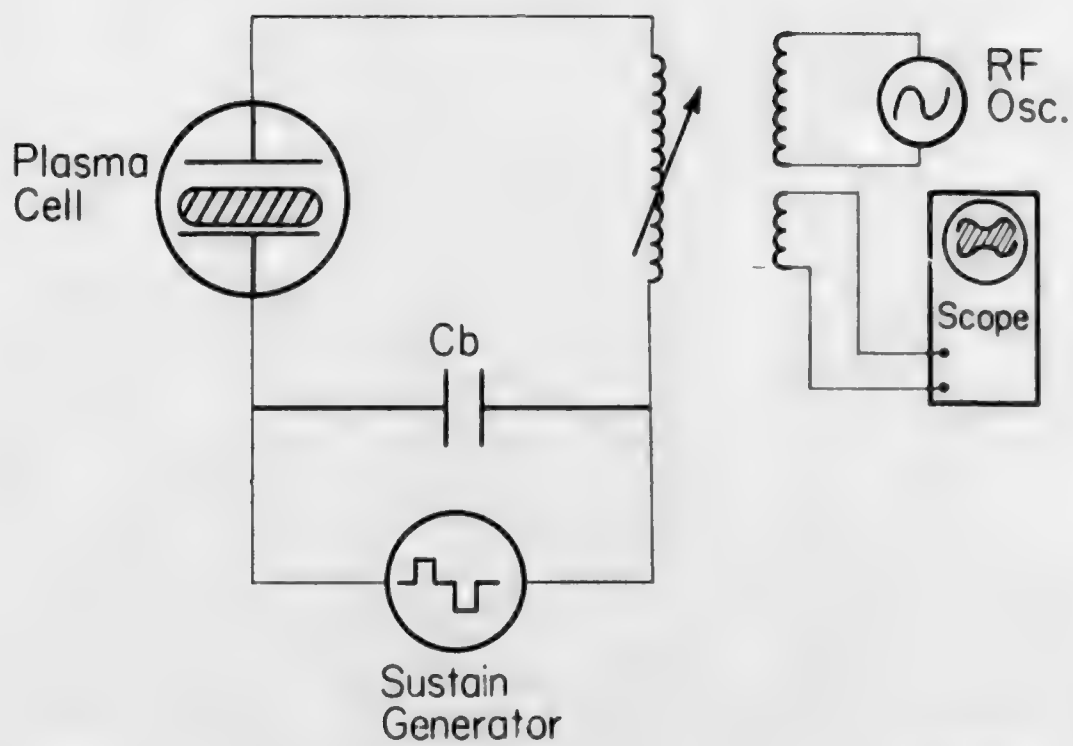
The existence of the plasma in the computer model stimulated the realization that the capacitance of the plasma cell should be varying as a function of the plasma. Figure 2.2 shows the density of the plasma is about 10^{-6} C/cm³ or about 10^{13} electrons/cm³. This corresponds to a plasma frequency of about 50 GHz. Thus for frequencies considerably below this, the plasma will appear as a material having a near infinite dielectric constant. This will change the capacitance of the cell as shown in Figure 2.4. Before the discharge, there is no plasma and the capacitance is the neutral value C_0 . At the discharge time t_d , the cell is filled with plasma and the capacitance is at a maximum value C_p . As the plasma decays the capacitance decreases until the plasma is gone and the initial C_0 value is restored. Thus a measurement of the capacitance of a cell gives information about the spatial extent and the existence of the plasma. Note that at the frequencies where such capacitance measurements are conveniently made, no information is obtained about the plasma density since these frequencies are much lower than the plasma frequency.

Figure 2.5 shows a simple method of measuring a capacitance change in a plasma cell. It is necessary that the capacitance measuring circuit elements not disturb the application of the sustain voltage to the cell. Also the sustain voltage signal should not cause excess noise to



CS-029

Figure 2.4. Plasma cell capacitance as a function of time due to the growth and decay of the plasma region.



CS-830

Figure 2.5. Resonance technique for measuring plasma cell capacitance.

obscure the capacitance measurement. For these reasons it is usually convenient to use a rf signal in the range of 10 to 100 MHz. In the Figure 2.5 circuit, a resonance is achieved between the variable inductor and the capacitance of the plasma cell. The capacitor C_b is large compared to the cell capacitance but small enough so as not to overload the sustain generator. The variable inductor must be small enough so as not to cause significant ringing when the sustain generator rises. The oscillator and the oscilloscope are loosely coupled to the tuned circuit by the small inductors. This technique is very sensitive to small capacitance changes if the Q of the LC circuit is very high. Thus it is particularly useful for measuring the capacitance changes in standard plasma panels where the small cell capacitance is in parallel with the many stray electrode capacitances making the relative capacitance change very small.

Figures 2.6 and 2.7 show the discharge current and the rf envelope measured with the circuit of Figure 2.5 on a standard 128-33 Digivue panel. The envelope waveform is strongly dependent on the frequency of the oscillator. Figure 2.6 shows the oscillator tuned to resonate with the neutral capacitance value C_0 . When the discharge occurs, the increased capacitance tunes the circuit out of resonance with the oscillator. At a slightly different oscillator frequency, Figure 2.7 shows the changing capacitance tuning the circuit in and out of resonance. Note that for this particular standard plasma panel, the capacitance is still changing, 15 microseconds after the discharge. This is excellent experimental proof of the existence of the plasma predicted by the computer calculations shown in Figure 2.2.

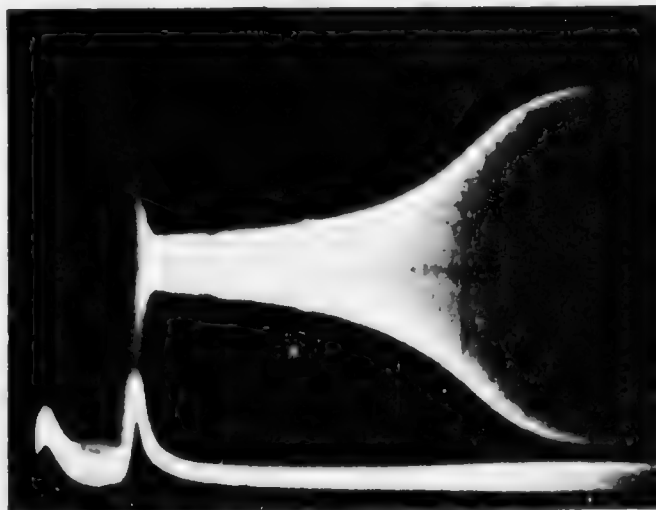


Figure 2.6. RF envelope of 19 MHz signal in upper trace. Discharge current at 40 ma per division in lower trace. Horizontal scale: 2 μ s per division. Data taken with circuit of Figure 2.5 on standard 128-33 Digivue panel.

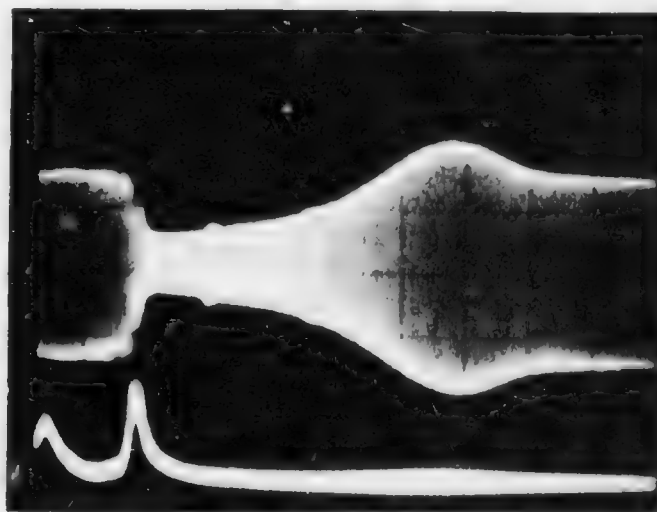
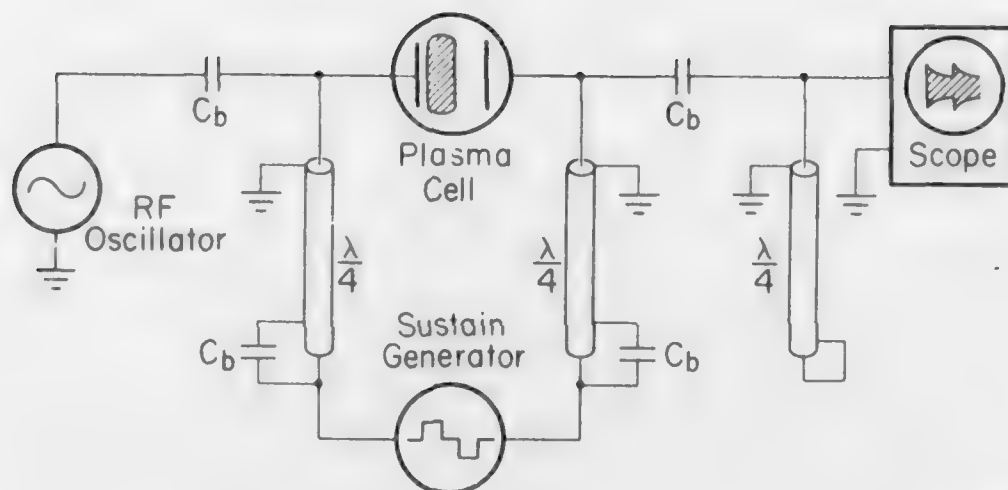


Figure 2.7. Same conditions as Figure 2.6 but with rf oscillator slightly detuned.

The circuit of Figure 2.5 has a few disadvantages. It is noisy since the rise of the sustainer always causes a considerable amount of ringing. This may die out in a few microseconds, but it obscures the discharge region. A second disadvantage is the complex relationship between the envelope amplitude and the capacitance that depends strongly on circuit Q and oscillator frequency. To solve these problems, the circuit of Figure 2.8 was used. Quarter wave stubs are used to isolate the sustainer from the plasma cell at the rf frequency. The capacitors of value C_b , are large enough to act as a short circuit at the rf frequency, but not overload the sustain generator. The final quarter wave stub, at the oscilloscope, effectively filters out the sustain generator frequencies but lets the rf frequency pass. Thus at the rf frequency the circuit behaves as if one lead of the cell is connected to the rf generator and the other to the oscilloscope. Because of oscilloscope capacitance, the measured signal is a voltage division between this capacitance and the cell capacitance. With the knowledge of the oscilloscope probe capacitance, the actual cell capacitance can be easily calculated.

To reduce the problem of the stray capacitances that usually shunt out the desired cell capacitance, a very large area cell having disc shaped electrodes 1 cm in diameter was constructed. The dielectric glass layer was about 25 μm thick and the cathode-anode gap spacing about 200 μm . Figure 2.9 shows the output waveform obtained from this special cell by means of the circuit of Figure 2.8. Note that the plasma exists for almost 60 μs after the discharge. This time varies with gas mixture and pressure. The longest time observed was 100 μs . As a general rule



CS-816

Figure 2.8. Circuit diagram of quarter wave stub technique for measuring the cell capacitance variation.

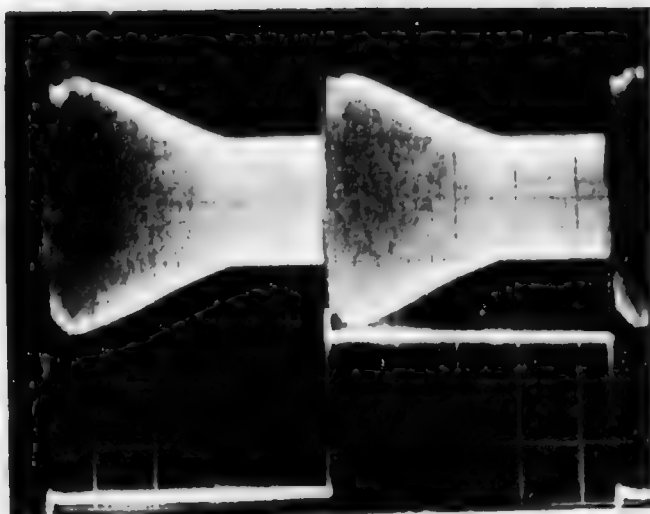


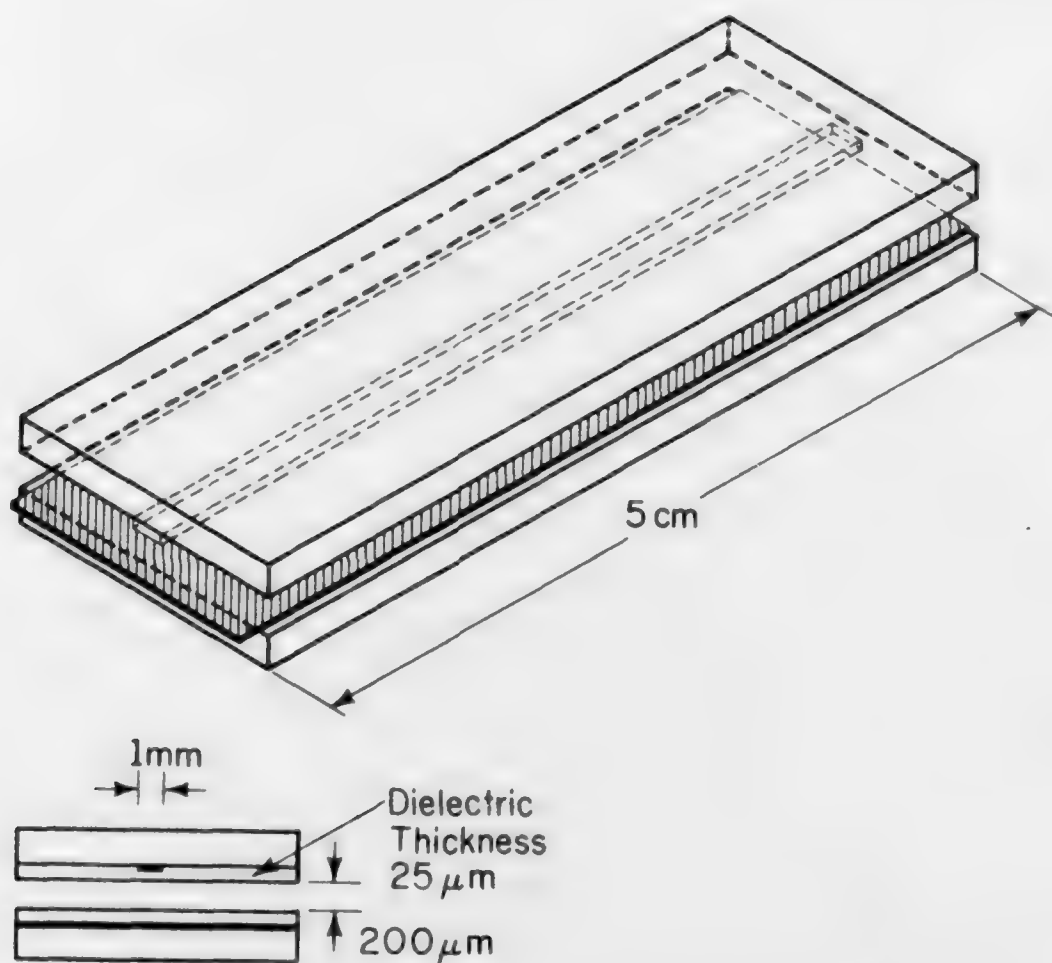
Figure 2.9. RF envelope of 57 MHz signal in upper trace. Sustain voltage waveform at 50 volts per division in lower trace. Horizontal scale: 20 μ s per division. Data taken with circuit of Figure 2.8 on special 1 cm diameter plasma cell containing 250 torr Ne and 0.25 torr Xe.

neon-xenon mixtures have a considerably longer plasma lifetime than neon-argon mixtures. This can be attributed to the diffusion and recombination coefficients of the minority gas ions.

The actual capacitance values of the cell can be determined from the data shown in Figure 2.9. This again varies with gas pressure and mixture, but typical values, referring to Figure 2.4, are 7 pf for C_0 and 50 pf for C_p . From these numbers one can estimate that at the peak, the plasma fills more than 6/7 of the cathode-anode gap. This is in agreement with calculations such as those shown in Figure 2.2.

2.4 Microwave Measurements

Although the capacitance is a relatively easy quantity to measure, it gives virtually no information about the density of the plasma. For this one must go to the higher frequencies. This means microwave or optical frequencies. Because the wavelength of the microwaves is very much larger than typical plasma cell dimensions, a very special cell structure must be used. Figure 2.10 shows a plasma cell that acts as a microwave strip transmission line. The impedance of this line is about 50 ohms. The sustain generator is connected between the ground plane electrode and transmission electrode by means of a very thin high impedance wire. 10 GHz microwaves were sent down the strip line, and the output was detected to show the transmission characteristics. Figure 2.11 shows typical microwave transmission data along with simultaneously measured low frequency capacitance measurements. The microwave transmission is very effectively cut off after the discharge. After 20 μ s the transmission begins to pickup until it has nearly perfect transmission after 50 μ s.



CS-832

Figure 2.10. Microwave stripline plasma cell.

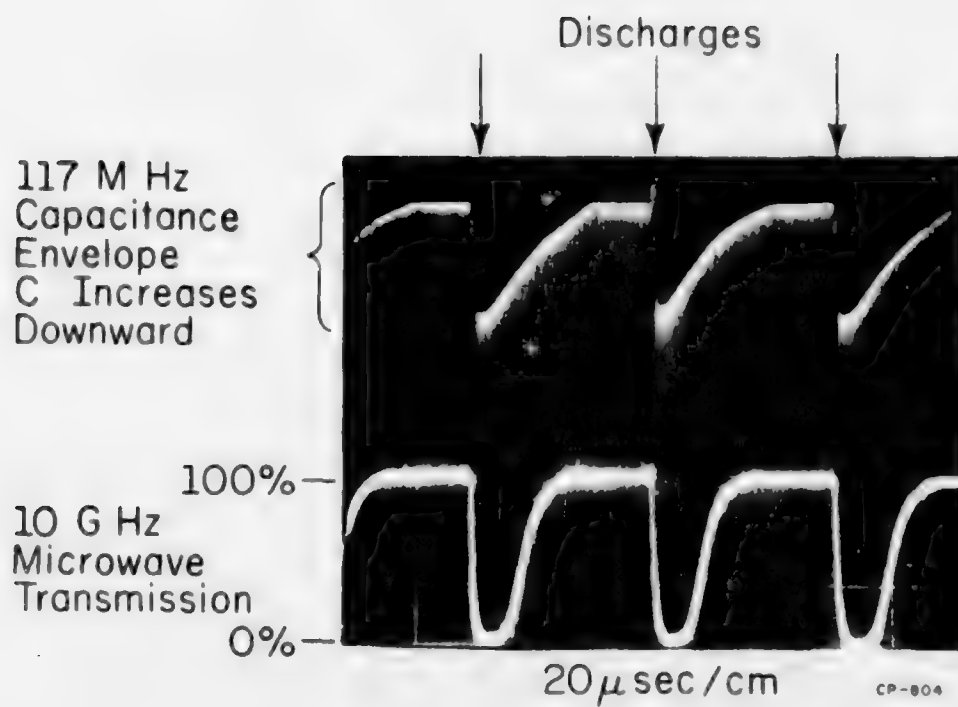


Figure 2.11. Microwave transmission data in lower trace and low frequency capacitance envelope in upper trace, for strip line cell shown in Figure 2.10, containing 250 torr Neon and .4 torr Argon. Horizontal scale is 20 μ sec per division.

The interpretation of this data is complicated since the transmission coefficient should be dependent on both the plasma density and its spatial extent throughout the gap. However one might roughly estimate that when the transmission is cut off the plasma density is great enough so that its plasma frequency is greater than the 10 GHz microwave frequency. This would indicate that the density is greater than 10^{12} cm^{-3} . However this estimate is further complicated by the fact that absorptive losses due to the plasma collisions with the neutral gas atoms can be very significant at the pressures typically used for plasma panels. Thus much additional data at other microwave frequencies is needed.

2.5 Optical Interferometry

One attractive method of measuring electron density as a function of time and space in the AC plasma display panel is optical interferometry. The basic principal is that the presence of electrons in a volume will when solving Maxwell's equations, cause electromagnetic radiation to propagate at a different velocity. For optical frequencies this is traditionally recognized as an index of refraction change. When light is sent through the plasma all of a given length, the light will experience a slight phase perturbation that can be measured by an interferometer.

The optical interferometry method of measuring electron density has a number of advantages over other techniques. It usually does not disturb the plasma such as do electric probes or microwaves. It can make very fast temporal measurements usually only limited by optical detector speed. Optical beams can be focused to a small point whose diameter is

limited by diffraction theory and thus they offer excellent spatial resolution. Microwaves, on the other hand, have a wavelength very large compared to a plasma cell and thus offer practically no spatial resolution at all.

2.5.1 An Accurate Interferometer

The prime question that needs answering is does the electron density in a plasma panel have sufficient amplitude to be measurable by interferometry techniques? From Maxwell's equations we get the well known relations that

$$\epsilon_r = n^2 = 1 - \frac{\omega_p^2}{\omega^2} \quad (15)$$

where ϵ_r is the relative dielectric constant, n is the index of refraction, ω_p is the electron plasma frequency, and ω is the frequency at which the measurement of ϵ_r is made, in this case the frequency of the probing light beam. It is also well known that ω_p varies as the electron density such that

$$\omega_p = \left(\frac{n_e e^2}{\epsilon_0 m_e} \right)^{1/2} \quad (16)$$

where n_e is the electron density, ϵ_0 is the dielectric constant of free space, e is the electron charge and m_e is the electron mass. For optical frequencies and the densities encountered in this work $\omega \gg \omega_p$ so that the following approximation can be made

$$n \approx 1 - \frac{1}{2} \frac{\omega_p^2}{\omega^2} \quad (17)$$

from (16) and (17) it is seen that for a given ω , Δn is proportional to Δn_e . Now if the light beam traverses a path of length L , the phase shift expressed in radians is

$$\Delta\varphi = 2\pi L(\Delta n - 1)/\lambda \quad (18)$$

where λ is the wavelength of light. From (16), (17), and (18) we find that

$$\Delta\varphi_e = -B\Delta n_e L\lambda \quad (19)$$

where $B = \frac{e^2}{4\pi\epsilon_0 c^2} = 2.817 \times 10^{-15}$ meters, c being the speed of light in vacuum.

Now from the numerical calculations of Section 2, we found that the peak electron density should be in the range of

$$10^{12} < n_e < 10^{13} \text{ cm}^{-3}.$$

If we assume a very long plasma display cell of 1 cm and a typical laser wavelength of 6328 Å, from (19) and an electron density of 10^{12} cm^{-3} we get a phase shift of 1.78×10^{-5} radians or 0.018 angstroms. This is a very small phase change that looks very discouraging since it is generally considered that good interferometry technique can only measure fringe shifts of $\frac{\lambda}{100}$, [11]. The basic problem that limits the sensitivity of most interferometers is mechanical stability. The mechanical elements usually move many angstroms due to thermal expansion and sonic vibrations.

There are two factors that created great optimism in being able to measure the required small fringe shifts. The first was the use of a particular type of interferometer in which most mechanical

motion was seen by both legs of the interferometer, thus canceling out to a relative motion of zero. The second factor was that since the plasma display panel operates at high frequencies (50 KHz) relative to the acoustic vibrations, much of this acoustic noise can be filtered and also averaging techniques are convenient to use thus greatly increasing the signal to noise ratio.

The Jamin interferometer arrangement used in this work is shown in Figure 2.12. The two optical flats are aluminized on their back sides to form mirrors. The beam from the laser is initially split by the surface reflections of the glass. The detector used in these experiments was a high speed photodiode. This interferometer is very simple in that there are only two elements that can move to cause an unwanted phase change - the two flats. Translational motion of the flats in the y and z directions causes no change in optical path length for perfect optical flats. For motion in the x direction, both the light beam going through the plasma cell and the reference beam experience the same path change and thus their relative phases remain unchanged. The only motion that can cause a noise signal is a rotational motion about the z axis. Thus this is an extremely stable interferometer. Most other interferometers such as the Michelson require a very stable mechanical mount to get the output fringes to remain stationary enough for the eye to recognize them. The Jamin interferometer meets this criteria when the flats are held with the human hand.

With the mechanical noise problem essentially solved, other noise sources become important. The light source becomes the main

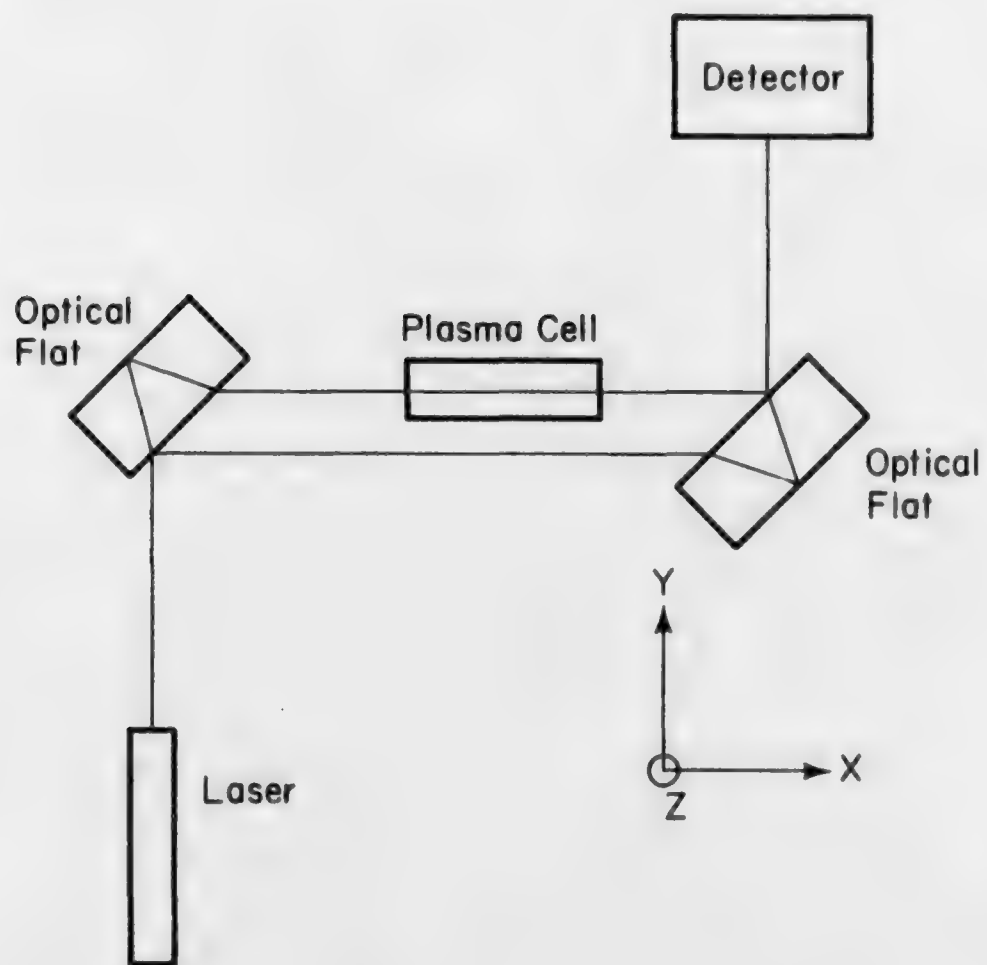


Figure 2.12. Jamin interferometer arrangement.

problem. Lasers are generally very monochromatic with bright and well collimated beams so that they are the only possible choice of light source for this problem. However, they are also fairly noisy devices. A 1% noise level may seem good to a laser manufacturer, but for this problem it represents a signal equivalent to a $\lambda/200$ phase shift and thus is quite unacceptable. Fortunately this noise can be canceled out by using a second detector and a differential amplifier. The second detector can be placed at a number of places along the beam. For instance in Figure 2.12 a beam splitter can be placed between the laser and the interferometer. The deflected beam from this beamsplitter goes to the second detector. The outputs of both detectors are fed to a differential amplifier. If the two detectors are sufficiently linear and properly frequency compensated, all of the excess laser noise can be canceled out to the level of the shot noise plus the detector noise. The shot noise is not the shot noise traditionally associated with the leakage current of the detector, but rather the shot noise due to the current from the laser light. This noise current is given by the familiar formula

$$I_{sn} = \sqrt{2 \Delta f I e} \quad (20)$$

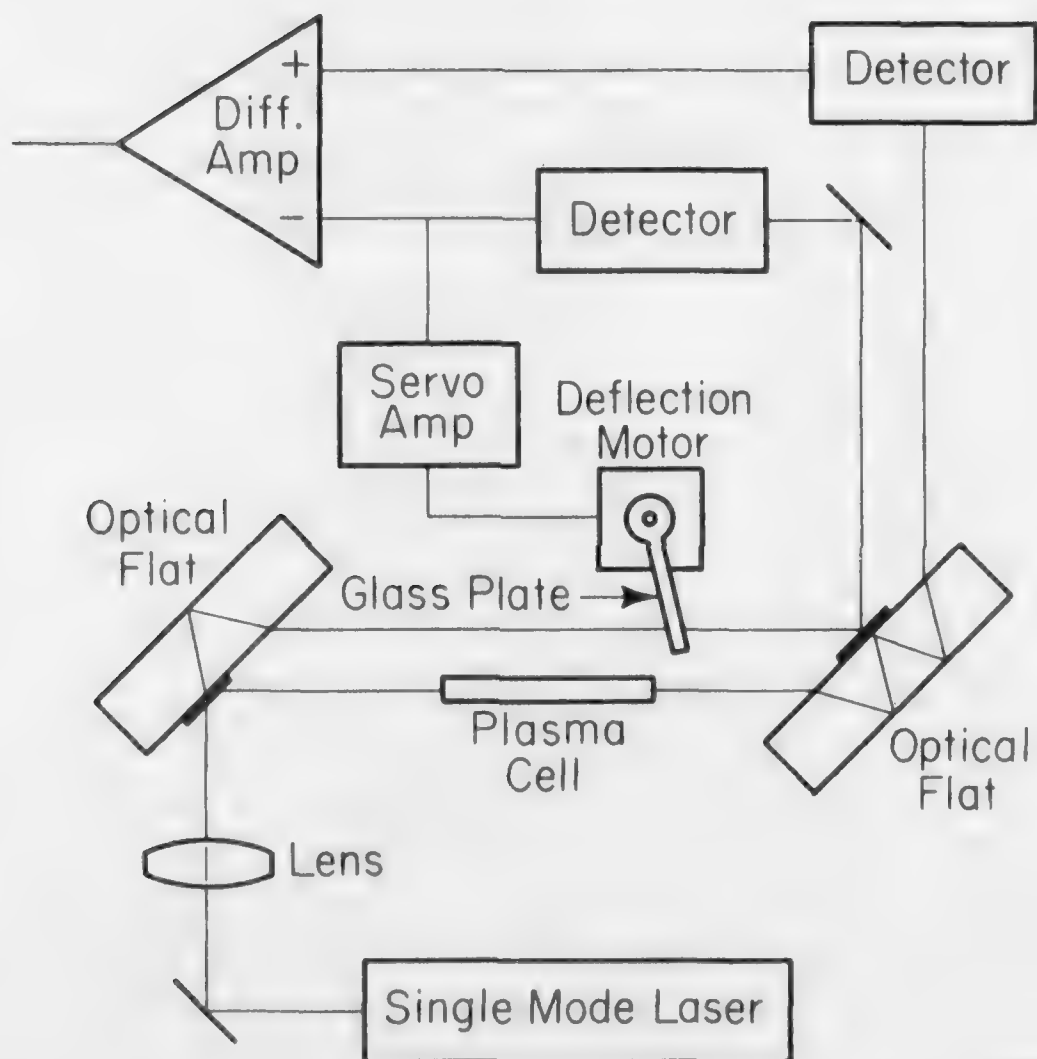
where Δf is the bandwidth, I is the signal current and e is the electron charge. Since the signal we wish to measure clearly increases proportionally to the laser light intensity, the signal to shot noise ratio increases as the square root of the laser intensity. Thus it pays to use the largest power laser available. A high power laser also eases the electrical noise problem since the electrical noise such as that due to

the high voltage sustain waveform is not dependent on laser power. Thus the signal to electrical noise ratio is proportional to the laser power. With the power from even a 1 milliwatt laser, the noise generated in the detector such as resistive noise is so small compared to the signal shot noise that all other noise sources can be neglected.

There are two basic improvements to the system of Figure 2.12 that improve the signal to noise ratio and the stability. To increase stability, a glass plate controlled by a servo system is placed in one leg of the interferometer. A change in the angle of the glass plate relative to the laser beam will cause the beam to travel a different length path through the glass. This is a very old trick that allows one to change the relative phase of one beam over the other and thus position the output fringes at the proper spot. If the flats are parallel to each other, the aperture of the laser beam will allow only part of one fringe to show up at the detector making the detector output approximate the amplitude of a single point in space while the fringes move by. This amplitude shows up as the familiar $\cos^2(\pi \frac{\Delta}{\lambda})$ relation where Δ is the optical path difference between the two interferometer beams. Since the fringe movement measured in these experiments is very much smaller than λ , the relationship between the phase change and the detector output can be assumed linear. The proportionality constant is determined by where along the \cos^2 curve one operates. The angular position of the glass plate determines this operating point. For maximum signal to noise ratio, this operating point should be where the \cos^2 curve has maximum slope. This occurs whenever $\cos^2(\pi \frac{\Delta}{\lambda}) = 1/2$. This is also the operating point where the linearity approximation holds

the best. It should be noted that the sign of the proportionality constant can be either positive or negative, depending on which preferred operating point is chosen. This fact serves as a helpful check for determining if the measured signal is a real phase change or some sort of electrical noise. Since the phase change signal can be inverted simply by slightly moving the glass plate, and since any electrical noise is most probably independent of the position of the plate, the noise and the signal can very easily be separated.

As discussed above, the Jamin interferometer is very stable; however over a period of minutes, small temperature changes can cause it to slightly drift. Also room air currents passing through the interferometer can cause one leg to have a slightly different optical length than the other. Most of these effects have frequency components that are much lower than those of interest for this work, however, these disturbances change the operating point along the \cos^2 curve and thus modulate the signals at the higher frequencies. For instance, if signal integration techniques are used to improve the signal to noise ratio, a number of minutes might be needed for the integration. Any drift of the operating point due to thermal change would cause a false signal to appear after the integration. Thus a servo system is needed to hold the interferometer to a fixed operating point. As shown in Figure 2.13, the glass plate is connected to a deflection motor which in this case was a simple speaker coil arrangement. The coil was driven by a servo amplifier with one differential input connected to the detector output and the other to a variable voltage source. When operating properly, the glass plate



CS-817

Figure 2.13. Interferometry system for measuring very small index of refraction changes in plasma cells.

rotates until the voltage output from the detector is equal to the variable voltage source. Thus by adjusting this voltage source, one can determine the operating point of the interferometer.

The deflection motor-glass plate arrangement had a natural resonance at 120 Hz. The servo amp had a computer aided designed 5 pole RC low pass filter with a rolloff very close to 12 Db per octave. Since oscillations in the servo system are undesirable, the gain of the amplifier was adjusted so that the gain at the 120 Hz resonance was just under 1. Thus the frequency response of the servo system does not affect the desired signals which all have frequency components above 1 KHz, but is fast enough to cancel out variations due to rapidly moving air currents.

A second improvement over Figure 2.12 is the addition of beam-splitters on the front surface of the flats as shown in Figure 2.13. This serves to increase the signal to noise ratio. From the above discussions, it is clear that when shot noise is limited, the signal to noise ratio will be improved the greater the signal at the detector. Also the signal at the detector should be fully modulated by the interferometer. Another way of saying this is that when the interferometer is adjusted for a minimum, the input to the detector should be zero. In Figure 2.13 the laser beam is initially split by the reflectivity of glass surface. For the proper polarization and a flat at 45° to the beam, the reflectivity of the glass surface is approximately 10%. Thus the two beams are not of equal intensity. When the two beams are recombined, the stronger beam that goes through the plasma cell only experiences a 10% reflection, and thus most of the laser energy does not reach the detector. What does reach the detector is 100%

modulated, but its maximum intensity can only be about 20% of the laser beam intensity. The addition of 50% reflecting beamsplitters at the points of surface reflection as shown by the darkened areas on the front of the flats in Figure 2.13 neatly solves this problem. This makes both beams of nearly equal intensity. The output to the detector is 100% modulated and the maximum signal to the detector can be nearly 100% of the laser signal. However, as stated above the interferometer is properly biased when the output is at half maximum so that only half of the laser energy goes to detector 1. It is convenient to place a second detector where the remainder of the energy goes. This is designated detector 2. If the outputs of both of these detectors are fed into a differential amplifier, the laser noise canceling function can be performed. Detector 2 essentially does the job that a beamsplitter and detector arrangement between the laser and the interferometer did as discussed above. Such a beamsplitter would have to deflect energy out of the interferometer and thus reduce the signal to noise ratio. The arrangement of Figure 2.13 allows the total laser power to enter the interferometer, along with the added advantage that the laser noise canceling detector also has a signal. With proper care, the signals entering the two detectors will be 180° out of phase, whereas the laser noise will be in phase, thus the output of the differential amplifier will show only the signal plus the shot noise. The balancing of the signals to the detectors is achieved by adjusting the glass plate position. For ideal beamsplitters with 50% reflection and transmission, the two output beams will be exactly balanced at the correct bias point.

The lens shown in Figure 2.13 is used to focus the laser beam in the area of the plasma cell to achieve optimum spatial resolution. The length of the plasma cell was chosen to be about 1 cm, which allows a reasonable compromise between the signal size and the desired spatial resolution. The longer the cell, the larger the signal according to equation (19). However, diffraction theory limits the length over which the beam can stay focused. For the beam to stay focused over 1 cm, the beam waist had to be made about 25 μm in diameter. A shorter length would allow a smaller beam waist. However the 25 μm resolution seems initially satisfactory for the 150-200 μm gap spacings used in typical plasma cells.

The system shown in Figure 2.13 was developed specifically for measuring these small phase shifts. The two optical flats define the basic Jamin interferometer which has the desirable property that translational motion of the flats changes the length of both optical paths equally, thus making the output signal invariant to mechanical vibrations. Each of the flats has a small dielectric beamsplitter on the front surface so that the two optical paths have equal intensity. Thus a half wavelength phase change in one path can cause 100% modulation of the output beam. A glass plate is inserted in one optical path and is rotated by a servo system to make slight corrections for low frequency thermal drifts and air currents. Both of the beams exiting from the output flat have the phase change information plus laser generated noise. However the phase change information is 180° out of phase between the two beams whereas the laser noise is in phase. Thus the output of the differential amplifier shows only the

optical phase change signal. A lens is placed in front of the interferometer so that the beam waist is in the center of the plasma cell, increasing the spatial resolution of the system to the diffraction limit.

To test the ability of this system to measure small phase changes, a CS_2 Kerr cell was placed in the interferometer to give a measurable phase shift. In a system that used a Spectra Physics 166 argon ion laser with an intra-cavity etalon, and an output power of nearly 1 watt at 5145 \AA , the measurements shown in Figure 2.14 were made. This shows a 50 KHz voltage applied across the Kerr cell and the resulting signal from the differential amplifier. This is a single oscilloscope trace recorded in real time without the use of any averaging techniques. It shows that resolutions of better than 0.1 \AA are obtainable without any trouble. The noise seen is due to the laser beam shot noise and also due to very small angular rotations of the laser beam due to laser vibrations. When signal integration schemes are used, phase shifts smaller than 10^{-5} \AA are readily observed with 10 seconds of averaging. Thus this interferometer is very sensitive and simple. To our knowledge this is the most accurate interferometer ever devised for the measurement of small phase shifts.

2.5.2 Interferometric Measurements on Plasma Display Cells

A plasma cell is constructed with electrodes of the geometry shown in Figure 2.15. A visible laser beam can be focused to a diameter of about $25 \text{ }\mu\text{m}$ over a 1 cm path. The cell which is made long so as to maximize the phase change is moved relative to the laser beam to determine the phase changes at various points along the gap.

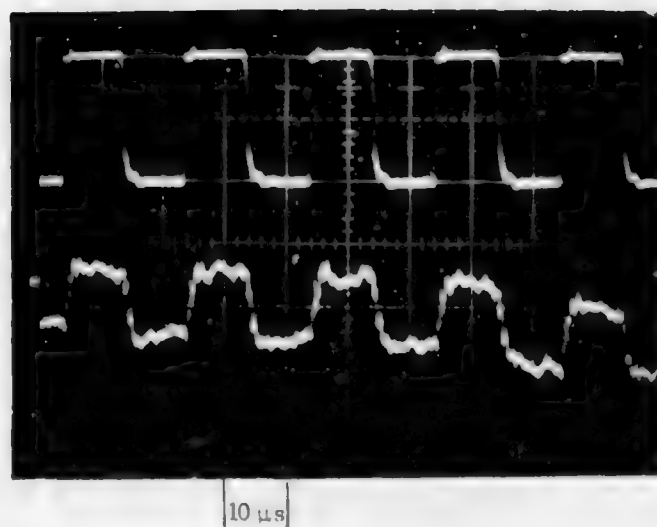
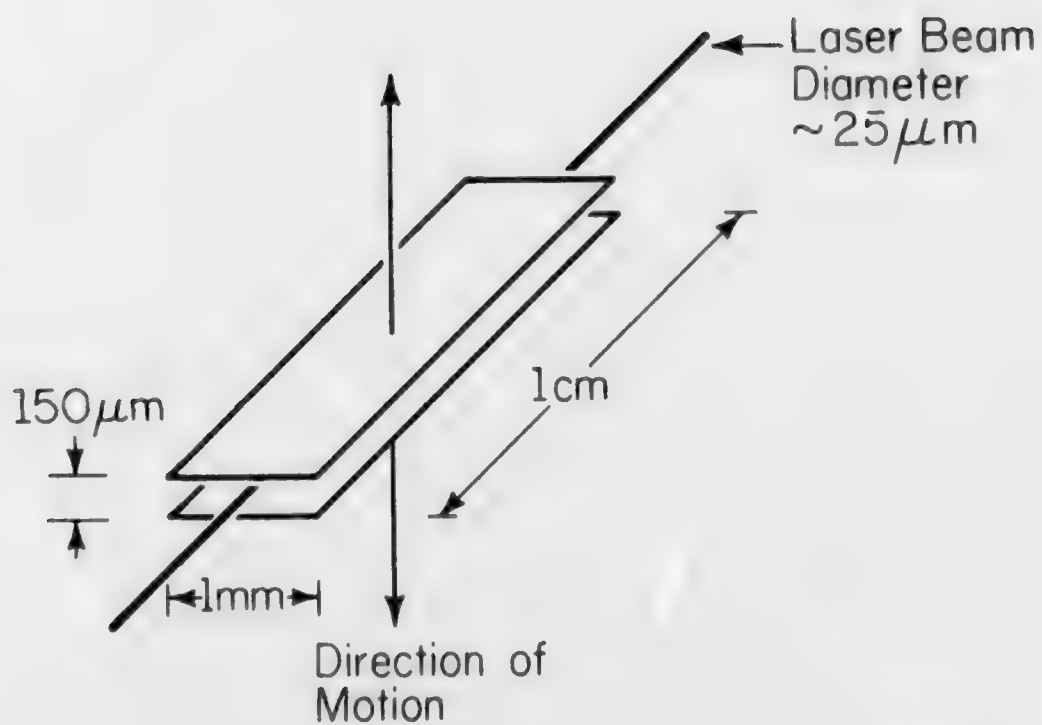


Figure 2.14. Voltage, in upper trace, applied to the Kerr cell to obtain the optical phase shift measured in the lower trace by the interferometer of Figure 2.13. Vertical scales: 20 volts per division and 0.1 \AA per division. Horizontal scale: $10 \text{ } \mu\text{s}$ per division.



CS-828

Figure 2.15. Basic geometry of plasma cell electrodes used in interferometry experiments.

Figure 2.16 shows typical phase change results obtained with an argon ion laser in a cell with electrodes with approximately the geometry shown in Figure 2.15. The beam is positioned at the center of the discharge gap. Each discharge of the cell is seen to initiate a series of strong oscillations that damp out with time. These phase changes are not typical of electron density changes but rather of neutral atom density changes. In a simple analysis, there are two density changes that can be measured by measuring the phase change of transmitted light. The phase change of the electrons, which behaves as described by Equation (19), and the phase change of the neutral atoms which behaves as Equation (18) where the change in the index, Δn , is proportional to the change in density of atoms. Thus the total phase change in radians is

$$\Delta\phi_{\text{tot}} = \frac{2\pi L(\alpha(\Delta N_a) - 1)}{\lambda} - B\Delta n_e L\lambda \quad (21)$$

where α is the proportionality constant between the atomic number density N_a , and the index of refraction for the particular gas atom. α can be easily found from knowledge of the index of refraction of the gas, n , at a given temperature T and pressure p by the relation $\alpha = \frac{np}{KT}$ where K is Boltzman's constant. α is slightly dependent on wavelength depending on the dispersive characteristics of the gas. It is not easy to separate the two effects. The standard solution used by most researchers is to perform the measurement at a number of wavelengths and because of the wavelength dependence of the two terms, there is a possibility of separating them.

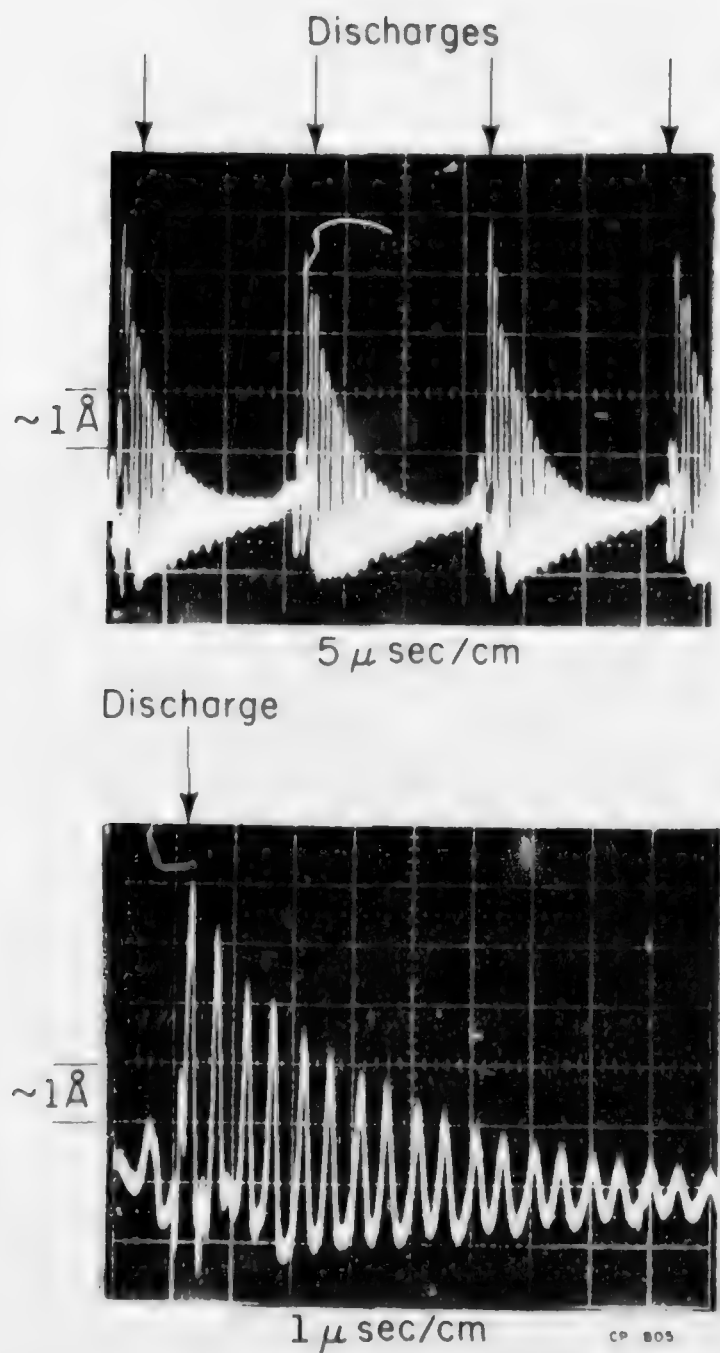


Figure 2.16. Typical phase change results obtained with an Argon ion laser.

The measurement of plasma display cell phase changes shown in Figure 2.16 shows rapid phase changes that are primarily due to atomic density changes. The density changes are due to sound waves that are initiated by the gas discharge. These sound waves travel back and forth from the anode to the cathode for many cycles before they are damped out by absorption. The exact nature of these sound waves can be determined by noticing the phase changes for different positions along the discharge gap. Figure 2.17 shows the cell discharge current and the phase changes for five differing positions along the discharge gap. The lowest trace shows the discharge current. Progressing upward, the next trace shows the phase change at the cathode. The third trace shows the phase change 54 μm from the cathode. The remaining traces are spaced by 54 μm , the top trace being at the anode. From the calculations of Section 2, it was seen that most of the discharge activity occurs near the high field region of the cathode. The hot electrons near the cathode will of course locally heat the neutral atoms. The more energetic neutral atoms will fly out of the cathode region and thus cause a decrease in density. This decrease is very clearly shown as a strong decrease in the index of refraction at the cathode at the time of the discharge. The impulse of atoms flying out of the cathode region sets up a sound wave that is first seen a short distance away from the cathode as an increase in index of refraction. The sound wave travels through space and time until it hits the anode in the top trace and is reflected back to the cathode. This bouncing between the cathode and anode continues for many microseconds as shown in Figure

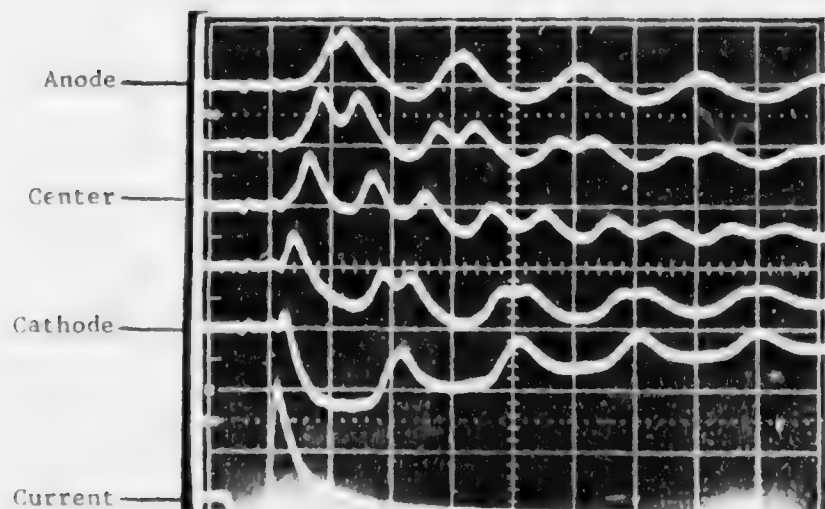


Figure 2.17. Multiple exposure photograph showing the index of refraction at 5 points along the discharge gap, as a function of time. The lowest trace is the discharge current at 10 ma per division. The bottom index of refraction trace is at the cathode and the top trace is at the anode. The intermediate traces are spaced by $54 \mu\text{m}$ intervals. Horizontal scale: $.5 \mu\text{s}$ per division. Vertical scale: 5 \AA per division.

The question arises as to how much of the phase change shown in Figures 2.16 and 2.17 is due to electrons. Clearly the rapid oscillations are due to the neutral density changes since the waves observed in Figure 2.17 travel at the velocity of sound. However, Figure 2.16 shows lower frequency components that may be due to electron density changes. To check this the interferometer was operated with a home built HeNe laser that oscillated simultaneously on 6328 \AA and $1.15 \text{ }\mu\text{m}$. From Equation (21), the ratio of the neutral change to the electron change should be ~ 3 times smaller at $1.15 \text{ }\mu\text{m}$ than at 6328 \AA . Thus any electron phase changes that are observable in Figure 2.16 should show up much more strongly at $1.15 \text{ }\mu\text{m}$. The sensitivity of the interferometer with the few milliwatts coming from the HeNe laser, was considerably less than that shown in Figure 2.16. However with a boxcar integrator, the phase changes due to the shock waves could be resolved as good as shown in Figure 2.16. As closely as could be measured, the phase changes in radians were inversely proportional to wavelength for the two wavelengths. Thus to the resolution of Figure 2.16, all of the phase change is due to neutrals. This is not too surprising, since calculations presented above showed that an electron density of 10^{12} cm^{-3} should yield a phase change of only $\sim 10^{-2} \text{ \AA}$. The data shown in Figure 2.16 is scaled at $\sim 1 \text{ \AA}$ per division. Thus one could hardly expect to see an electron phase change even at $1.15 \text{ }\mu\text{m}$ with this resolution. The neutral atom phase changes seem to amount to a 5 \AA shift. Thus there could easily be a ratio of 500 between the neutral and electron phase shifts. To separate these two by a two wavelength experiment will require an accuracy of the measurements much greater than given by oscilloscope

traces and even the boxcar integrators, due to dynamic range limitations. Measurement of electron densities, even with the sensitive interferometer setup described above, is difficult. This problem will be discussed further at the end of this section.

2.5.2.1 Atom Density Measurements

We first consider what can be learned about the discharge from our ability to measure very accurately the neutral atom density in space and time. A basic assumption that was used in all calculations presented in Section 2 was that the neutral atom density was constant. This is of course an approximation, but how good of an approximation? From Equation (21) and Figure 2.16, it can be easily calculated that a 5 Å phase shift represents only a $2.0 \times 10^{16} \text{ cm}^{-3}$ change in density. Since the atomic density at 250 torr and 25°C is $8.84 \times 10^{18} \text{ cm}^{-3}$, it is seen that the perturbations are clearly very small, making the constant density approximation a good one for the neon + 0.1% Xe mixture. This is probably not true for all gas mixtures, however. An example is shown for 250 torr xenon. Pure xenon is an attractive choice for color plasma display panels that use the ultraviolet light generated by the xenon to excite phosphors [12]. Figure 2.18 shows the sound waves for a cell with 250 torr xenon. The sound waves give about a quarter wavelength phase change. Such a large phase distorts the approximate linear relation between the phase change and the output of the interferometer, however the \cos^2 relationship still exists. This large phase change is partially due to the fact that the index of refraction at STP of xenon is 1.000708 [13] whereas that of neon

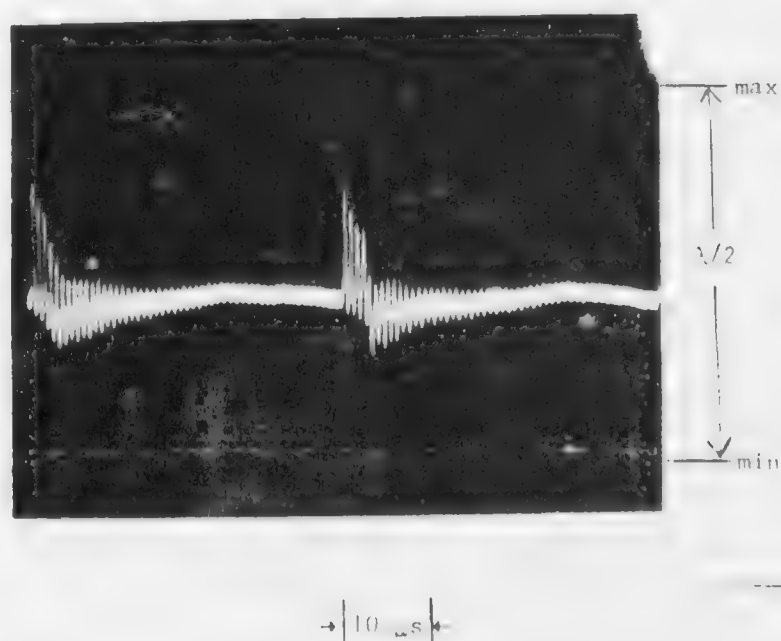


Figure 2.18. Optical phase changes for two discharges in cell with 250 torr Xe.

is only 1.0000673 [14]. However the atomic density change due to the sound waves in xenon is also very much larger than that of neon. The data of Figure 2.18 shows density changes as great as 10% of the equilibrium density. The approximation of uniform neutral density starts to breakdown and thus the effects of the soundwaves must be included in discharge calculations.

The measurements presented above show only the high frequency changes in neutral atom densities. There is, however, a steady state change that occurs whether the cell is on or off. This density change is due to the competition of the heating of each discharge and the thermal relaxation or cooling of the gas. Thus this steady state change is established after a number of discharges and is also strongly dependent on the repetition rate of the discharges. To measure this, the cell was effectively turned on and off by interrupting the sustain generator for many cycles. Such data is shown in Figure 2.19. In this figure, the cell which was initially sustained at a 50 KHz rate was turned off by stopping the sustainer. The neutral density quickly increases to its equilibrium value in a few hundred microseconds. After the equilibrium value is reached, there are still small fluctuations due to soundwaves traveling long distances through the entire cell structure. After 9 milliseconds of interruption, the sustainer was again applied and the discharges caused a new steady state value to be achieved. The wide band structure of the second half of the trace is due to all of the soundwaves bouncing between the anode and cathode similar to Figure 2.16. Figure 2.20 shows data for the same experiment but with only a 1 millisecond sustainer interruption.

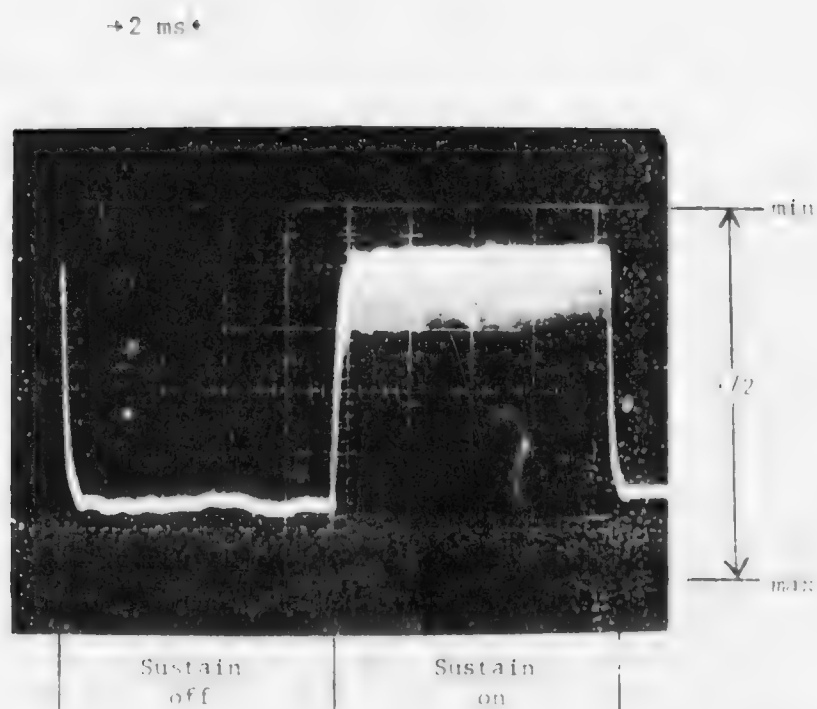


Figure 2.19. Phase changes in Xe filled cell showing slow density changes due to slow gas temperature changes.

The time constant for the relaxation of the gas density to equilibrium appears to be about 100 μ s. Figure 2.21 shows data for even a shorter time scale where the interruption of the sustainer was only about 150 μ s. In this case the cell never reaches a steady state situation. The sound waves reflecting between the cathode and anode are clearly visible here. With each discharge the neutral atom density decreases slightly due to the additional heating that each discharge introduces.

The thermal conductivity of neon is much greater than that of xenon so that the cell reaches steady state much more quickly. However because of this greater thermal conductivity, less thermal energy can be stored in the gas and thus the neon neutral atom temperature much closer to the temperature of the glass wall. Thus the steady state density changes in neon are not as great as those for xenon. These density changes are observable, and have characteristics similar to those of Figures 2.19, 2.20, and 2.21 but with much smaller phase changes and much shorter time constants. However, due to the low frequency drift characteristics of the interferometer, it is not possible to get a good oscilloscope trace of this data for pure Ne.

The above mentioned measurements indicate the nature of the neutral density changes in the gas. These density changes are caused primarily by temperature changes in the gas. These temperature changes in the gas are indirectly measurable by observing the density changes that they cause. For instance, in Figure 2.17, the trace of the phase change at the cathode shows that at the time of the discharge, the index of refraction dropped sharply. This is a decrease in neutral density

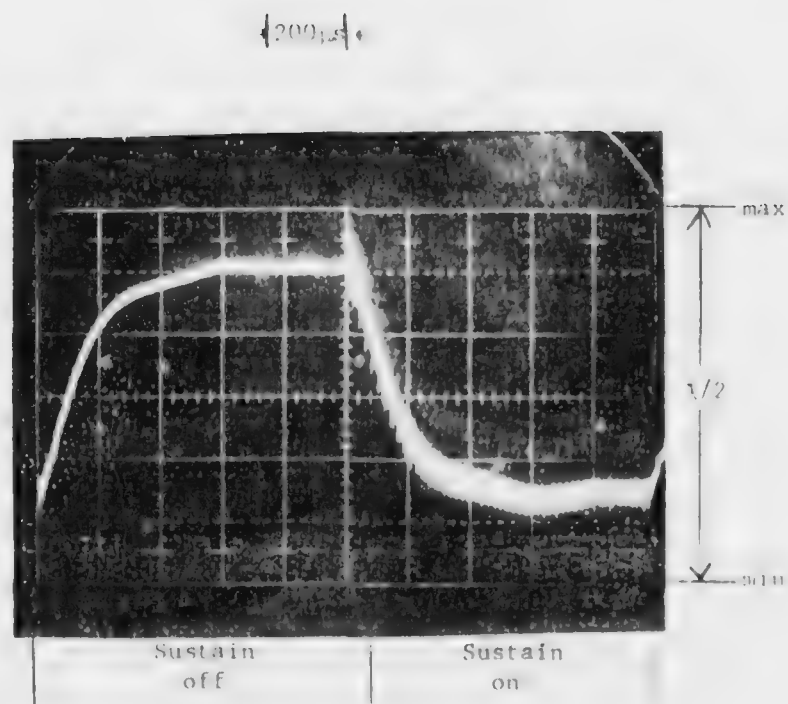


Figure 2.20. Same conditions as in Figure 2.19 but with time scale $200 \mu s/\text{div}$.

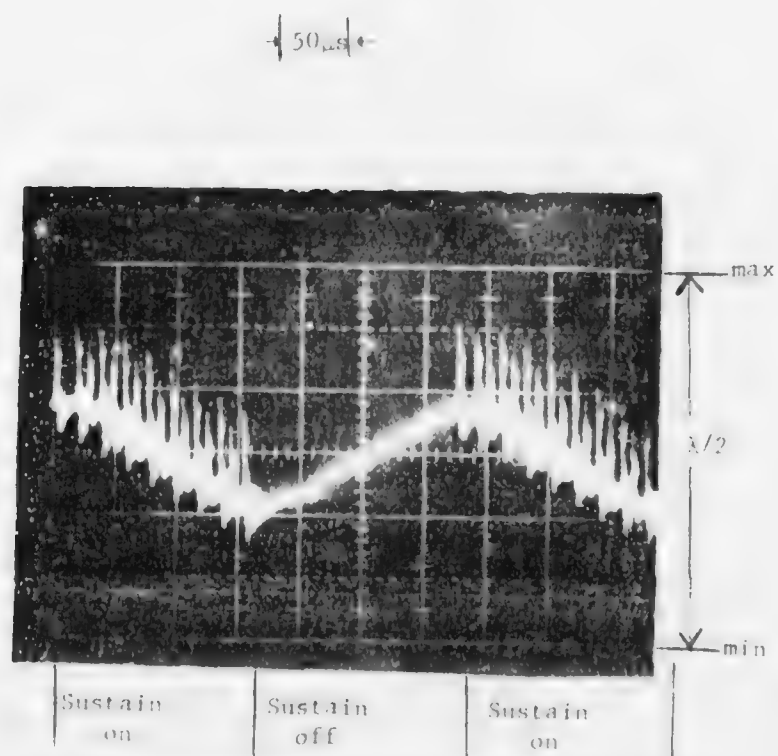


Figure 2.21. Same conditions as in Figures 2.19 and 2.20 but with time scale $50 \mu s/\text{div}$.

directly attributable to a sharp increase in temperature near the cathode region. The traces of Figure 2.17 for regions away from the cathode do not show this sharp drop at the time of the discharge and thus there is not much heating. One problem with this technique is that the sound waves also cause similar changes in neutral density. Thus it is a matter of judgment and care to come up with the current explanation for the observed phase changes. Nevertheless, this is a useful qualitative technique for observing the areas of heating, as will be discussed later in this section.

A second problem with measuring the temperature change by watching the neutral density changes is that one only finds out the temperature changes and not the actual temperature. As indicated in Figures 2.19, 2.20, and 2.21, it typically takes a number of discharge cycles before the gas comes to an equilibrium temperature. Thus a technique is needed to measure the absolute temperature of the gas. Fortunately a simple technique exists for doing this by measuring the velocity of the sound waves bouncing between the cathode and the anode as in Figure 2.17. The velocity of sound in a gas is proportional to the square root of temperature and very weakly dependent on gas pressure. The pressure dependence is too weak to be of concern for the following calculations. By measuring the time for the sound waves to make many cathode-anode transits, the velocity can be accurately determined with knowledge of the cathode-anode gap spacing. To make the temperature measurement less dependent on the gap spacing measurement, the sound wave velocity was measured at a number of different sustain frequencies. If the sustain frequency is very low like 1 KHz, then the temperature of the gas will be very close to the ambient of the glass walls.

This is true for most all gases since Figure 2.20 shows that even a low thermal conductivity gas like Xe reaches an equilibrium situation after a few hundred microseconds. Once the velocity is measured at 1 KHz, the sustain frequency is then increased to the desired value, e.g. 50 KHz. Because of the dependence of velocity on temperature, the following relationship holds for the two velocities and temperatures:

$$\frac{T_H}{T_L} = \frac{U_H^2}{V_L^2} \quad (22)$$

where T_H and V_H are the temperature and velocity at the high sustain frequency, and T_L and V_L are for the low sustain frequency. T_L is assumed to be the ambient temperature of the glass panel. The velocities are not actually measured, but some convenient transit time which is proportional to the velocity. This might typically be the time for 10 round trip transits of the sound wave.

One would expect that a cell filled with xenon should show the largest temperature changes since Xe has poor heat conductivity compared to the lighter inert gases, and also the discharge is much more intense in xenon. The transit times were measured with a 50 KHz sustainer and a 1.5 KHz sustainer. The results showed that the gas temperature at 50 KHz was 36°C above the temperature at 1.5 KHz which was assumed to be within 1°C of the ambient temperature of the glass. This was with 250 torr Xe and a 185 μ m gap spacing. This is the same cell arrangement used in Figures 2.18, 2.19, 2.20, and 2.21. Such a large temperature change is consistent with the ~ 10% density changes shown in Figure 2.19 at a constant pressure.

Thus in the case of pure Xe, the effects of average gas temperature are significant and must be included in any theory of operation.

For more standard gas mixtures such as Ne + 0.1% Xe, the temperature change is much smaller and is not detectable with the sound velocity technique because of limited oscilloscope resolution. The resolution limits show that the temperature increase cannot be greater than 5°C. If one assumes that the density change such as shown in Figure 2.19 is completely due to a change in temperature at constant pressure, then the temperature change in Ne + 0.1% Xe at 500 torr and a gap spacing of 185 μm is 3.5°C. Thus for typically used gas mixtures in plasma display panels, the gas is always within a few degrees C of the ambient glass temperature. This is not to say that the glass does not get above the room ambient. It is well-known that a fully lit plasma panel may rise 10 or 15°C above ambient. However the gas temperature will always be within a few degrees C of this warmer glass ambient. Thus any model of Ne filled plasma panels can justifiably neglect the effects of neutral gas temperature change.

2.5.2.2 Electron Density Measurement

The laser interferometry technique seems to be an excellent measure of the neutral atom density in the plasma display panel. However, these interferometry experiments were performed in hopes of measuring the electron density, a quantity much more important to the operation of the device. As shown above, the neutral density changes may be about 10^3 times bigger than the electron density changes. Since an electron density of 10^{12} cm^{-3} should give about a 10^{-2} \AA phase change for this experimental

setup, it is clear that the problem is not the signal to noise ratio of the system since, as shown in Chapter 4, 10^{-5} Å phase changes are above the noise level of this system for reasonable integration times. Thus in theory, the electron density is measurable if the electron and neutral densities can be separated.

The standard technique for separating these two densities is to perform the measurement at two different laser wavelengths as discussed above [15]. From Equation (21) it is clearly desirable that the two wavelengths (λ_1 and λ_2 , $\lambda_1 \gg \lambda_2$) be as far apart as possible in order to maximize the difference of the resulting phase changes. We can rewrite Equation (21) as

$$\Delta\varphi_{\text{tot}} = \Delta\varphi_a + \Delta\varphi_e \quad (23)$$

where $\Delta\varphi_a$ is the phase change due to neutral atom density changes and $\Delta\varphi_e$ is the phase change due to electron density changes. From (21) it is clear that

$$\Delta\varphi_a = \frac{A}{\lambda} \quad (24)$$

and
$$\Delta\varphi_e = E\lambda \quad (25)$$

where $A = 2\pi L(\alpha(\Delta N_a) - 1)$ and $E = -B\Delta n_e L$. Since from the above discussions, $\frac{\Delta\varphi_a}{\Delta\varphi_e} = 5 \times 10^2$, the value of A can be approximated from (23) and (24) by

$$A = \lambda_2 \Delta\varphi_{\text{tot}_2} \quad (26)$$

where $\Delta\varphi_{\text{tot}2}$ is the total phase change for $\lambda = \lambda_2$. From (23), (24), and (25) at the two wavelengths, one finds that

$$E = \frac{\lambda_1 \Delta\varphi_{\text{tot}1} - \lambda_2 \Delta\varphi_{\text{tot}2}}{\lambda_1^2 - \lambda_2^2} \quad (27)$$

Since $\Delta\varphi_e$ is so small compared to $\Delta\varphi_a$, the question of how accurate $\Delta\varphi_{\text{tot}}$ must be measured becomes very important. From (27) the accuracy of the E measurement is determined by the accuracy of the numerator since the wavelengths in the denominator are known to high precision. From (23), (24), and (25), the numerator of (27) is

$$\lambda_1 \left(\frac{A}{\lambda_1} + E\lambda_1 \right) - \lambda_2 \left(\frac{A}{\lambda_2} + E\lambda_2 \right) \quad (28)$$

or

$$(A + E\lambda_1^2) - (A + E\lambda_2^2) \quad (29)$$

Since A is very much larger than $E(\lambda_1^2 - \lambda_2^2)$ and $E(\lambda_1^2 - \lambda_2^2)$ is the sum of the two terms in the numerator of (27), a measure of the accuracy that the values of φ_{tot} must be measured is found by the ratio

$$\frac{E(\lambda_1^2 - \lambda_2^2)}{A}$$

which from (25) and (26) equals

$$\left(1 - \frac{\lambda_2}{\lambda_1} \right)^2 \left(\frac{\Delta\varphi_{e1}}{\Delta\varphi_{a1}} \right) \quad (30)$$

from the wavelength assignment convention $\frac{\lambda_2}{\lambda_1} < 1$. Also from the data presented here $\frac{\Delta\varphi_{e1}}{\Delta\varphi_{a1}} < 0.002$. Thus the value of (30) is also less than 0.002. This value represents the accuracy with which $\Delta\varphi_{\text{tot}1}$ must be known for the error in $\Delta\varphi_{\text{tot}1}$ to give a false value of E equal to the real value of E in (27). Thus for greatest accuracy, one should try to maximize (30).

For signal to noise reasons an argon ion laser has been chosen for these experiments. In order to maximize (30) it is desirable to choose λ_1 and λ_2 as far apart as possible. For the available laser power the choice is $\lambda_1 = 5145 \text{ \AA}$ and $\lambda_2 = 4579 \text{ \AA}$. For $\frac{\Delta\varphi_e}{\Delta\varphi_a} = 0.002$, this gives a value of 4.16×10^{-4} . Thus for the expected values of $\Delta\varphi_e$, and the available laser, $\Delta\varphi_{\text{tot}}$ must be measured to an accuracy of better than 4 parts per 10^4 . Since from the data of Figure 2.17, $\Delta\varphi_{\text{tot}}$ is typically 5 \AA , this measurement requires a resolution of at least $2 \times 10^{-3} \text{ \AA}$. This is clearly within the resolution of the interferometry system which is better than 10^{-5} \AA . However, such resolutions require the use of a boxcar integrator for the necessary averaging. These instruments usually only have a dynamic range on the order of 10^3 . Thus the noise of the system will be determined by the noise in the boxcar integrator, even when the $5 \text{ \AA} \Delta\varphi_{\text{tot}}$ input gives the maximum output on the boxcar integrator.

One approach to this problem relies on the ability to remove the electrons from the gas volume by placing appropriate voltage waveforms on the cell. Small voltage pulses placed on top of the sustain waveforms have the effect of sweeping the plasma out of the volume. The idea is to subtract a discharge cycle with plasma from a cycle in which the plasma

was removed. If the only difference in the two signals is the removal of the plasma, then the plasma signal should show up clearly in the difference. This technique is now being developed.

2.5.3 Glass Surface Properties

All of the above experiments were directed at measuring properties of the gas volume. Of equal importance are physical effects at the glass cathode surface. A major question that is still debated is what proportion of electrons are generated by photon, ion or metastable atom bombardment of the cathode. It has previously been reasoned that only photon bombardment was important because the speed of the discharge processes was faster than the ion process. [16,17,18] This reasoning is false since most of the computer calculations performed in this work used only the ion effect and achieved times as fast and faster than the experimentally measured discharge times.

To resolve this issue, an experimental cell was made with a glass cathode. A pulsed light source was focused on the glass cathode to photoemit a pulse of electrons. With gas in the cell, and the appropriate dc voltage, the electrons initiate Townsend avalanches which are measured with a sensitive current detector. These avalanches lead to succeeding avalanches by means of the photon, ion, or metastable bombardment. Because of the grossly different speeds of these three effects, it is usually a simple matter to separate them in time. Figure 2.22 shows a single trace of avalanches produced by a single light pulse. For experimental reasons, the cell had a very large gap spacing and thus a

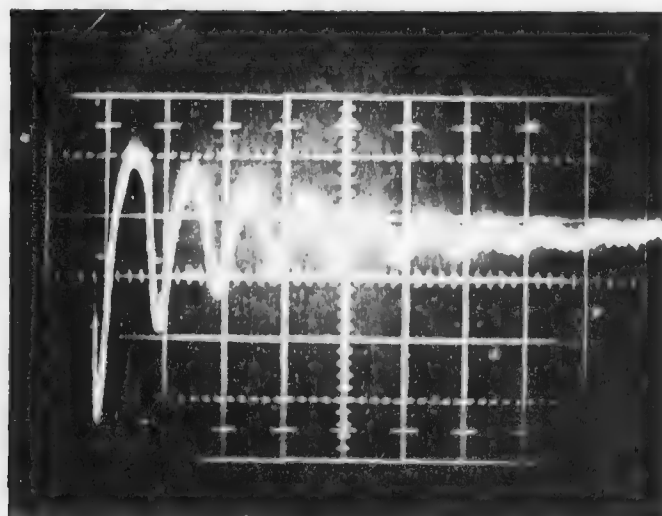


Figure 2.22. Avalanche currents in a glass cell having an electrode separation of 2.5 cm and filled with 5 torr Ne and 0.25 torr N₂. Vertical scale: 5×10^{-9} Amps per division. Horizontal scale: 50 μ s per division. The current increases downward.

necessarily low gas pressure. The glass cathode was made of common window or soda glass. The avalanches were clearly regenerated by the ion effect for this data. The period of the avalanche group shown in Figure 2.22 corresponds to the ion transit time across the gap. After a number of avalanches, diffusion processes cause the individual avalanches to be obscured. However they continue until enough current has flown to charge the glass surface and reduce the voltage across the discharge gap. All of these experiments were performed with the applied dc voltage very close to the breakdown voltage. No successive avalanches due to photon bombardment were observed. In certain gas mixtures, such as pure neon, the ion processes were accompanied by a much slower growth process that appeared to be attributable to metastable bombardment.

III. INTERNAL LOGIC

3.1 Introduction

One of the most important implications of the gas discharge studies is that it should be possible to enhance the internal logical capability of the plasma display panel without degrading performance. This section provides a background for multilevel internal decoding, it describes a new technique for multilevel writing, and it relates these results to complementary investigations in process at other laboratories.

3.2 Panel Decoding

In a matrix display panel containing $m \times n$ elements, a binary message of $(m+n)$ bits must be decoded to select a specific element for writing or erasing. Although all of this decoding can be performed rather simply by circuitry external to the panel, this approach requires a control circuit for each element, and except for some specialized large area displays with modest information content it is not economically practical. A 512×512 display, for example would require 262,144 control circuits and at least the same number of connections to the panel.

If the display elements have appropriate characteristics, one level of decoding can be performed in the panel itself, and as a result, the complexity of interconnections and external circuitry can be reduced significantly. In the AC plasma display panel, for example, each display element functions both as a storage cell and as a logical "and" element. For an $n \times n$ panel the number of addressing circuits is reduced from n^2 to $2n$, and for a 512×512 panel, in particular, from 262,144 to 1024.

The next level of decoding is usually performed by external circuitry which either selects an active element connected to the selected row or column electrode, or else provides a submatrix of logical "and" elements through which row or column selection is made by a smaller number of active elements. For a 512×512 panel the "and" elements can be grouped for each axis in a 32×16 submatrix and can be driven by 48 active elements.

Although the circuit problem is manageable, better compatibility between panel and circuitry can be achieved if the panel itself can provide one more level of decoding. A 32×16 submatrix of additional "and" elements for each axis within the panel requires only 48 addressing circuits instead of 512. If this reduction in external circuitry is not offset by increased panel complexity, the total cost of the display panel and its required circuitry can be substantially reduced. We describe several ways of increasing the internal logical capability of the display panel, with a view toward reducing overall costs.

The essential structure which, with variations, is basic to this entire class of techniques replaces each row or column electrode by a pair of electrodes, and interconnects these electrodes in two sets of groups such that selection of two groups on an axis selects both electrodes of only one electrode pair. For a 512×512 panel the electrodes on each axis are divided into 32 groups for one set, and 16 groups in the second or orthogonal set. The electrodes are driven by the external circuitry through 48 connections. The principles of this arrangement for a 9×9 array are shown in Figure 3.1. In this figure selection of group A and group a selects both electrodes of only one line pair.

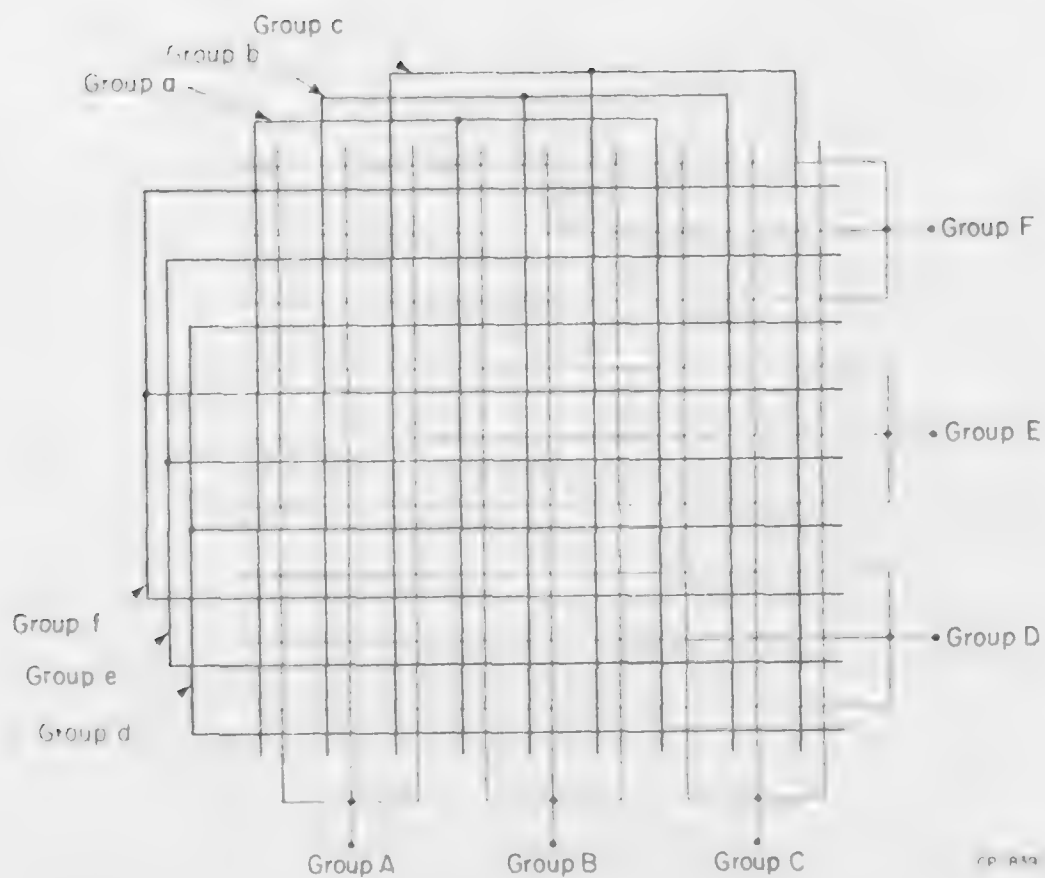


Figure 3.1. Electrode arrangement for Four Input Internal Logic.

The simplest approach to addressing in this structure to provide a second level of decoding was based on the idea that if a write signal were applied simultaneously to both electrodes in a pair the line pair would be fully selected, and at the intersection of two fully selected line pairs there would be an initiating discharge. If a write signal were applied to only one electrode of either pair there would be no initiating discharge. Unfortunately this configuration behaves more as a logical "OR" circuit than as a logical "AND" circuit since the voltage on either electrode, or both could establish breakdown. (Because of the wider electrode area provided by two electrodes, the breakdown would occur at a somewhat lower voltage than with one electrode, but the margin for addressing would be small.)

A more promising variation of the double electrode approach uses a metallic ring or a transparent conducting dot to average the voltages that are applied to the corresponding electrode pair. The dots (or rings) are insulated from the electrodes by a thin dielectric layer that covers the electrodes and are insulated from the gas by a second dielectric layer. However, because each element functions as a linear mixer there is a three quarter select condition which does not appear in a logical "and" circuit and which could reduce operating margins. A further disadvantage to the system is the more complicated structure that requires registration of the averaging elements with the intersections during assembly. Nevertheless, this technique should function properly.

Schermerhorn's recently published discharge logic system retains the simplicity of the original structure and exploits the principle of discharge coupling to discriminate between full selection and partial

selection [19]. When two intersection line pairs are each fully selected for erase, terminating discharges at each of the four intersections end the discharge sequence only at the selected intersections in the element. In the following cycles coupling from the nonterminated discharges restores the discharge sequences at the remaining intersections.

Writing in this system, is produced by erasing, preceded and followed by a state inversion which in effect turns all "on" cells "off" and all "off" cells "on". In state inversion a bias voltage is, in effect, added to the sustaining voltage which offsets the augmenting effect of wall voltage. At the same time it increases the voltage across "off" cells causing them to ignite. This system has been demonstrated by Schermerhorn at Owens-Illinois [19]. For some applications the aesthetic problems of inversion and the slow write cycle caused by the two inversion steps make the technique unsuitable.

3.3 A New Technique for Writing

The challenge in discharge logic is to combine the simple erase technique of Schermerhorn's with an equally simple write technique. Hope for meeting this challenge is based in part on the fundamental work described in section 2 which indicates that ions and electrons formed during a discharge, or partially developed discharge, can remain in the gap for many microseconds, that the presence of these charges can accelerate the development of a subsequent discharge at the same location, and that these charges can be removed from the gap through appropriate pulsed voltages. It is also related to work at Fujitsu and at the U of I on shift

panels, and on the discharge logic work at Owens-Illinois which shows that the presence of a discharge at one location lowers the firing voltage at nearby locations [20,21].

In one implementation of the write technique pulsed voltages are applied to each electrode at a fully selected element. The voltages pulses, however, are not applied simultaneously, but instead are timed to appear across two of the intersecting electrodes for time T_1 and then across the remaining two intersecting electrodes for time T_2 . A partial plasma, established during the first interval T_1 , is drawn to the neighboring intersection during T_2 , and leads to a fully developed discharge. The discharge spreads on the next half cycle to cover all four of the electrode intersections at the selected element. Discharges should not develop at partially selected elements.

In a variation of this technique the initial select pulse height is increased to provide a more intense initializing plasma. (A narrow pulse of high amplitude provides an intense discharge without developing a large wall voltage.) For a fully selected display element the discharge spreads to the diagonal intersection. For a partially selected element, the tentative selection must be removed, either by removing the plasma if the wall voltage is small, or by creating a controlled discharge which, in effect, "erases" the portion of the display element that has been tentatively "written".

These techniques await the fabrication of experimental panels to be fully investigated. They are discussed here because the conceptions are results of the fundamental work, because they appear to be sound, and

because if successful they should provide one method of realizing significant cost savings through reduction of circuit complexity.

IV. SPATIAL GRAY SCALE

4.1 Introduction

In its usual applications the plasma display panel displays text and simple graphics. There are, however, many applications for which some degree of scale would be desirable. Probability density functions or other three dimensional mathematically defined surfaces could be displayed using light intensity variations rather than a perspective drawing. Simulations of population growth or heat distribution could be displayed in a similar manner. If a simple video input head were developed, pictures could be passed from one terminal location to another in a facsimile mode. In fact, with a digital video input device such as a CCD, CID, or photodiode array, there would be a direct geometric correspondence between the image and display permitting direct digitizing of image point locations on the panel.

In this section we review two methods of spatial gray scale generation, the results of a hardware realization of one of them (the ordered dither technique), and some research on methods of compressing the display image data.

4.2 Dot Density Methods

Unlike the CRT where each phosphor dot intensity can be varied directly, some other form of gray scale generation must be used with the bi-level plasma panel. The current gray scale methods fall into one of two categories; pulse frequency modulation or dot density techniques.

The time division methods [22-25], which include the multi-state, the multi-sustainer, and duty cycle modulation, vary the number of light output pulses per unit time at each display point to achieve gray scale. Because these methods require extensive panel sustainer modification, and thus are not compatible with existing panel displays, our work focused on dot density techniques.

Dot density gray scale relies on the spatial ratio of "on" points to total display points in a small panel region to represent intensity levels. Since each panel point is either "on" or "off" these methods can be displayed on any existing panel and lend themselves to computer software simulation. These methods can be classified into adaptive and nonadaptive groups. In adaptive methods the decision to turn a panel point "on" or "off" depends not only on the intensity of the original image at that point and possibly the position of the point in the array, but also on the character of the image in the neighborhood of that point. Nonadaptive methods use only the image intensity of the point and in some cases, the position of the point. Because of the complex nature of adaptive dot density routines, our research has emphasized only non-adaptive methods.

One of the simplest methods of generating gray scale displays on the panel uses a predetermined pattern of 1 (ON) points in a $N \times N$ array of panel points to represent $N^2 + 1$ levels. The algorithm computes the average of the picture element (pel) intensities in a $N \times N$ section of the input pels and maps the intensity onto the panel using the nearest fixed pattern level. Only $N^2 + 1$ patterns are required to generate any image, but

since N^2 pel intensities are averaged, as N increases, the resolution of the display decreases as $1/N$.

Computer simulations of the fixed pattern method were done using two picture files. One was a full gray scale picture with 64 levels of gray and the other was a high contrast black on white line drawing. The simulations show good resolution in the 5 level ($N=2$) display, but contouring is severe because of the limited gray scale. Although sharp details are missing, 17 levels ($N=4$) of intensity provide a good compromise between gray scale and resolution for the gray scale picture; but the line drawing is greatly distorted. The 8×8 pattern (65 level) display results in almost unrecognizable reproductions of both files due to the large area of video data being averaged. The problem of the fixed pattern method is the inability to faithfully reproduce high spatial frequency data.

The simplest means of generating a video display is through fixed reference threshold detection. If the input pel intensity exceeds the reference, the corresponding panel point state is set to 1, otherwise it is set to 0. For reproducing high contrast material such as line drawings or text, this technique works well, but for other input material all of the gray scale information is lost. However, if the reference is allowed to vary randomly over the full input intensity range for each pel comparison, a very "noisy" half-tone representation results [26].

While working with the problems of TV video data compression, Limb [27] introduced a deterministic signal which, when added to the digitized signal eliminated some contouring. It was evident that these

techniques could be incorporated on a bi-level display to generate gray scale. Known as the ordered dither technique [26], this algorithm compares each scaled input pel intensity with a predetermined, position dependent set of threshold values to determine whether the corresponding display point is a 1 or 0. The size of the so called dither matrix determines the number of distinct gray levels in the display (Figure 4.1). Because the pels are mapped onto the panel one to one, rapid intensity variations are preserved in the display. Ordered dither can reproduce regions of high and low spatial resolution without distortion or highly visible patterns [26,29].

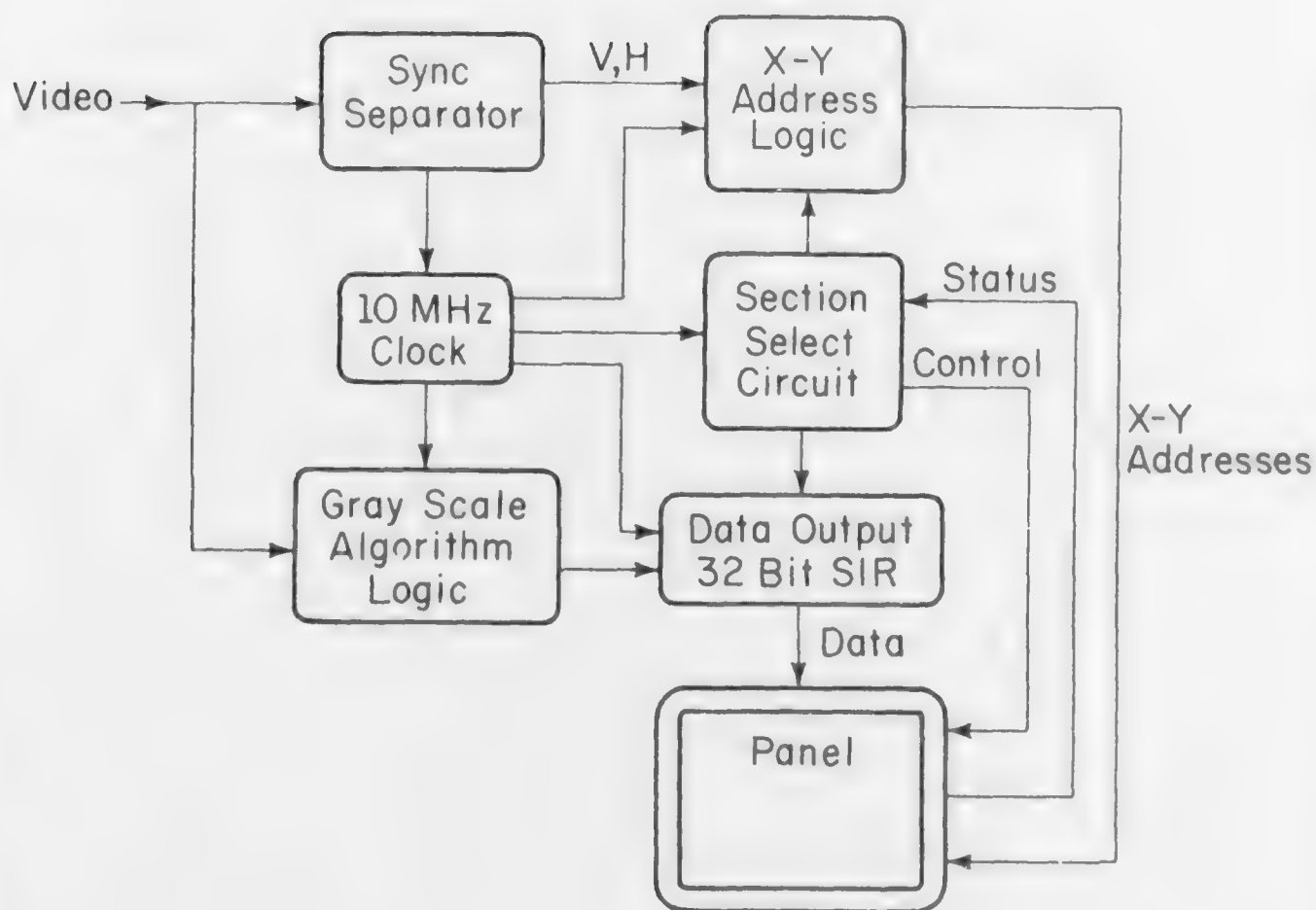
Computer simulations of ordered dither have shown this technique to be superior to the fixed pattern method in resolution and smooth gray scale transitions. Using ordered dither to generate the gray scale photograph and the line drawing demonstrates that even the 65 level reproductions display good resolution. It was also found that little improvement was noticed between a dither matrix of 8x8 (65 levels) and 16x16 (256 levels).

4.3 Hardware Implementation

Because of its inherent simplicity and the encouraging results, ordered dither was selected for implementation in hardware. An interface was designed to sample the video output of a standard vidicon camera and generate the necessary command words for a 16 bit parallel input plasma panel. (Figure 4.2) The interface divides a TV video frame into 16, 32 bit sections. 32 bits are sampled with a 10 MHz clock and sent to the panel

$$D_{2n} = \begin{pmatrix} \frac{4D_n}{4D_n + 3U_n} & \frac{4D_n + 2U_n}{4D_n + U_n} \\ 0 & 2 \\ 3 & 1 \end{pmatrix} \quad U_n = \begin{pmatrix} 1 & 1 \\ 1 & 1 \end{pmatrix}$$

Figure 4.1. The ordered₂dither matrix. Each D_n can represent N^2+1 intensity levels.



GP-949

Figure 4.2. Block diagram of drive circuitry.

during each horizontal line scan period, for a total display generation time of 550 ms [29].

Ordered dither can be generated in two ways. Either the video can be digitized and compared to a digital reference, or the reference level can be generated with a D/A converter and an analog video comparison performed. The second method was selected as the least complex, and a 6 bit digital to analog converter was constructed using a resistor ladder network and high speed transistor switches (Figure 4.3). An examination of the required position dependent dither levels revealed that they were simple functions of X and Y panel address. Logic circuits were designed and built to generate the proper binary codes for a 17 and a 65 level ordered dither matrix [29].

The complete imaging system processes the input video before it is packed and sent to the parallel panel. After viewing numerous types of source images, the real time system has been shown to perform as well as the computer simulations predicted it should. The system reproduces both full gray scale and black on white text well (Figure 4.4).

This video interface, constructed on five circuit cards using standard TTL devices, demonstrates that the hardware generation of video displays on the plasma panel need not be complex or costly.

4.4 Data Compression

The 16 bit parallel panel can write or erase 16 consecutive Y points each 20 μ s, and generate an entire 512x512 display in 327 ms, which is a data rate of 800K bits/second. Thus, to generate gray scale graphics in the least possible time, transmission lines with bandwidths

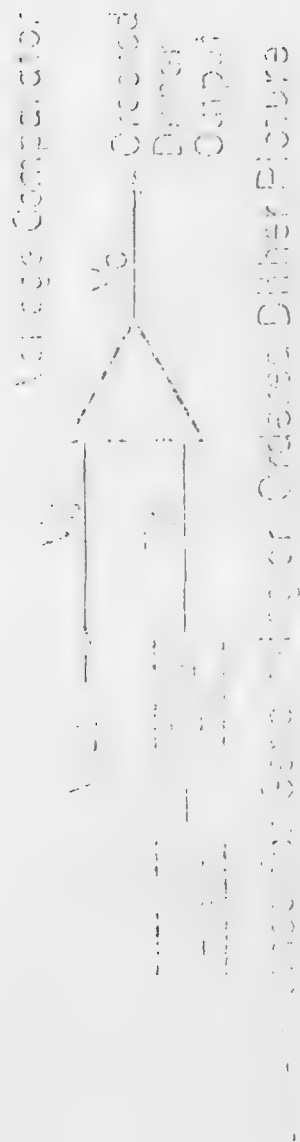


Figure 4.3. A system to generate ordered dither for the plasma panel interface.



Figure 4.4. An example of an image generated on a 512-60 Digivue using the ordered dither system.

much greater than 1200 baud telephone lines must be used if one is to transmit each bit of the display. However, since the higher bandwidth lines are available only at extra cost, some form of data compression is required to establish a compromise between line bandwidth and display generation time. Without the ability to display images in a reasonably short time over low bandwidth lines, and store those images in as little memory as possible, few applications will exist for panel graphics.

Four display files have been used in these simulations, each representing a different class of input. Two of these files, LADY and DEMO, are full gray scale generated with 65 level dither, one, IDIOT, is a black and white cartoon generated with dither, and the final file is a threshold detected version of the cartoon.

Run length coding has been used with success in transmitting threshold detected material rapidly.[28] Variable length codes have been shown to realize compressions of 2 to 4 display bits per transmitted bit, but these codes do not lend themselves to ordered dither because there are so many runs of only a few bits. Instead, a modified run length code has been devised known as the 4 bit linear pattern code [29] that locates 4 bit patterns in a line of the display and transmits the code word and number of consecutive occurrences. The results using this code are summarized in Figure 4.5 for several input files. It can be seen for all of these files that the compression ratio lies between 1.7 and 2.2. Thus this technique would reduce transmission time from 2.4 minutes to a maximum of 1.4 minutes. A maximum of 32 bits can be represented by each of the 8 bit code words, but even in the worst case the panel can keep up with the data on a 1200 bit/sec line.

PATTERN SIZE, $N \times M$

FILE	4×4	4×4^1	8×4	8×4^2	8×8	8×8^2	4-BLP
LADY	2.29	3.20	4.00	5.33	6.40	8.00	2.22
DEMO	2.00	2.29	3.56	4.57	7.11	8.00	1.77
IDIOT	2.29	2.67	3.56	4.57	6.40	7.11	1.81
IDIOT1	1.78	—	4.78	—	6.40	—	2.21

COMPRESSIONS RATIOS

- 1) Allow 1 bit error.
- 2) Allow 1, 2, or 3 bit errors.

Figure 4.5. Compressions ratios for the 4 sample files using the $N \times M$ pattern codes and the 4-bit linear pattern code.

The patterns generated in 2 dimensions were examined to determine whether special characters could be defined and displayed with character codes. With such characters, the display time would be nearly independent of the image composition once the character set were loaded. The effective compression ratio would be equal to the character size divided by the character code bit length. On a 1200 baud line, about 180 6 bit character codes could be sent per second for a full screen display time of 82 seconds for 4x4 characters and 21 seconds for 8x8 characters.

Investigation showed that very few patterns made up most of the display. As Figure 4.6 shows, the picture files have 10 962 4x4 arrays, each of which can assume any one of $2^{16}=65\,536$ values, but in two cases fewer than 75 patterns exist. Even an 8 bit code word reduces the storage by 50%. One can also see how many more patterns appear in the threshold detected file because it lacks the structure ordered dither places on each array. Similar results were found for 8x4 and 8x8 characters.

Due to the nature of dot density gray scale displays, a number of isolated bit errors can be accepted in the display before the picture quality is significantly impaired. Therefore, two patterns were combined if they differed by one Hamming distance, and the number of patterns were tabulated. In all files significant improvement was achieved, reducing the required number of 4x4 patterns to 29 in one case. In 8x4 and 8x8 characters 2 bit errors were permitted in patterns that represented less than .1% of the display, further reducing the necessary patterns to below 103 in all cases.

Display of the compressed picture files has demonstrated that the errors can be tolerated. These results suggest that a set of patterns

PATTERN SIZE, $N \times M$

FILE	4×4	4×4^1	8×4	8×4^1	8×4^2	8×8	8×8^1	8×8^2
LADY	71	29	251	124	60	599	387	195
DEMO	143	74	261	142	103	301	214	167
IDIOT	75	34	396	168	69	741	566	337
IDIOT1	451	—	687	—	—	603	—	—

NUMBER OF DIFFERENT PATTERNS

- 1) Allow 1 bit error.
- 2) Allow 1, 2, or 3 bit errors.

PATTERN SIZE

	4×4	8×4	8×8
Number of $N \times M$ Arrays in the Files	10962	5481	2709

TOTAL NUMBER OF ARRAYS

Figure 4.6. The number of different patterns found in each sample file.

and pattern codes could be used to store gray scale displays in perhaps 20% of the 262K bits required for a full panel bit by bit memory map.

V. SYSTEMS RESEARCH

5.1 Graphic Display Terminal/Host System Architecture Studies

The design of computer system architectures has been and will probably continue to be closely governed by the nature of the tasks that the system is required to perform. It seems clear that no single optimum arrangement of components and subsystems will provide for the wide variety of needs of the Navy. Although there will remain differences in overall architecture there are some subsystems which are required to exhibit similar characteristics from system to system. Important examples are the terminal and communication subsystems which will be used in future ground based computer-based information systems and computer-based instrumentation and monitoring systems in aircraft, submarines, and ships.

The primary purpose of a computer-based information system is to provide a user with rapid access to stored or computer generated information usually available from some central source, algorithm, or data bank. There are a considerable number of large information systems emerging at the present time through the Navy. These include ARPANET, Lockheed Information Services, systems which will supply maintenance and calibration support, both ground based and on-board education and consulting, as well as real time instrumentation and monitoring. In each of these systems however there is a common configuration emerging, forced both by technology and economics. It is basically that of a host system communicating in a conversational mode to a rather sophisticated intelligent graphics terminal over voice grade communication lines. In the large number of general systems one does not

expect this basic configuration to change radically even though the configuration of the host and the terminal may vary considerably because of changes in display technology, low cost mass storage, mini and microcomputers etc. It is not expected that the cost of bandwidth between host and terminal will drop in the near future, in fact the opposite will probably be the case. As a result, we have felt that it is important to continue to investigate ways in which the "apparent" bandwidth between the user and the host can be optimized. By this we mean ways in which the human interaction with the information can take place in a natural manner. We would like to emphasize that what is important in any information system is the efficient and economic transfer of information to and from the human requesting service. It is important that system designers and engineers recognize that, in the end, it is overall efficiency of information transfer that is the important parameter that needs to direct the system architecture. For example the increased productivity of users who can, in real time, manipulate models, monitor activity, access data and consult with an information bank through the use of an interactive graphics terminal is quite remarkable.

One basic result of our work in this area has been the development of a systems model which takes the form shown in Figure 5.1 and Figure 5.2. Figure 5.1 illustrates the arrangement which we feel will emerge in the case of large ground based systems even though remote terminals may be aboard ship. Figure 5.2 illustrates the general arrangement that seems to be emerging in the case of local instrumentation systems such as those used in future aircraft, submarines, and ships. In each case, it seems clear that significant cost performance benefits can be achieved by using terminal

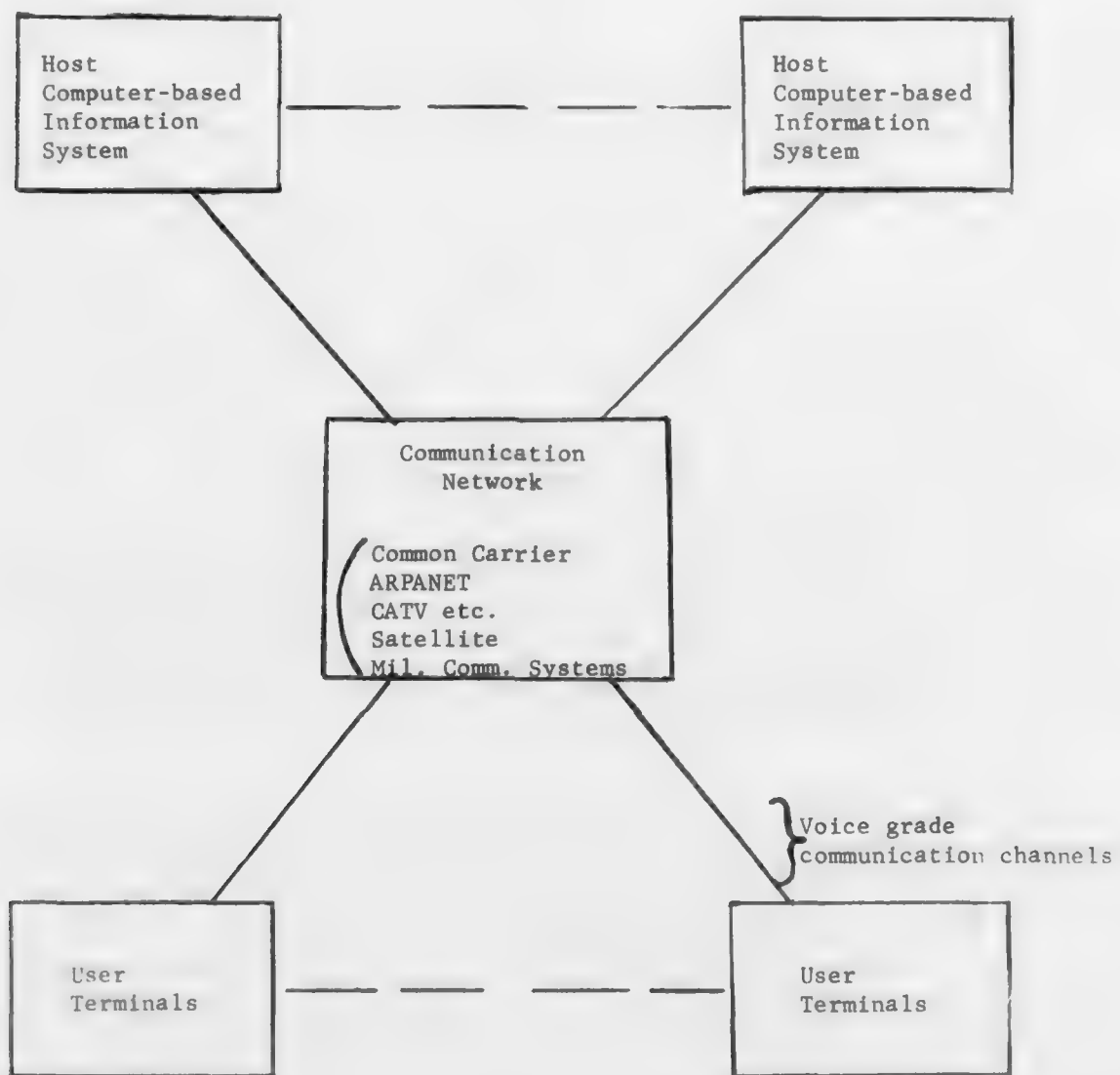


Figure 5.1. Architecture of a large computer-based information system.

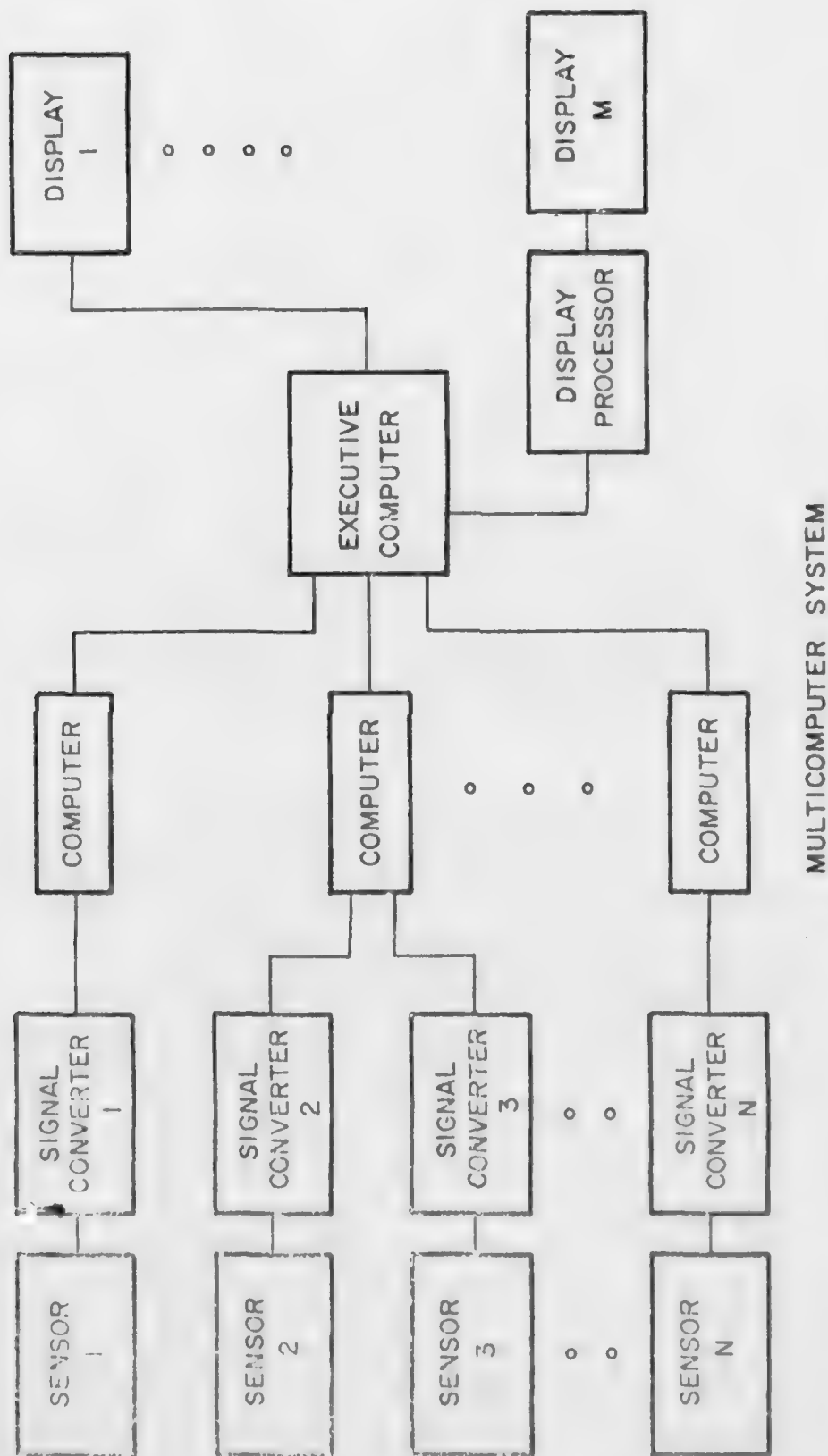


Figure 5.2. Architectures for future computer-based instrumentation systems.

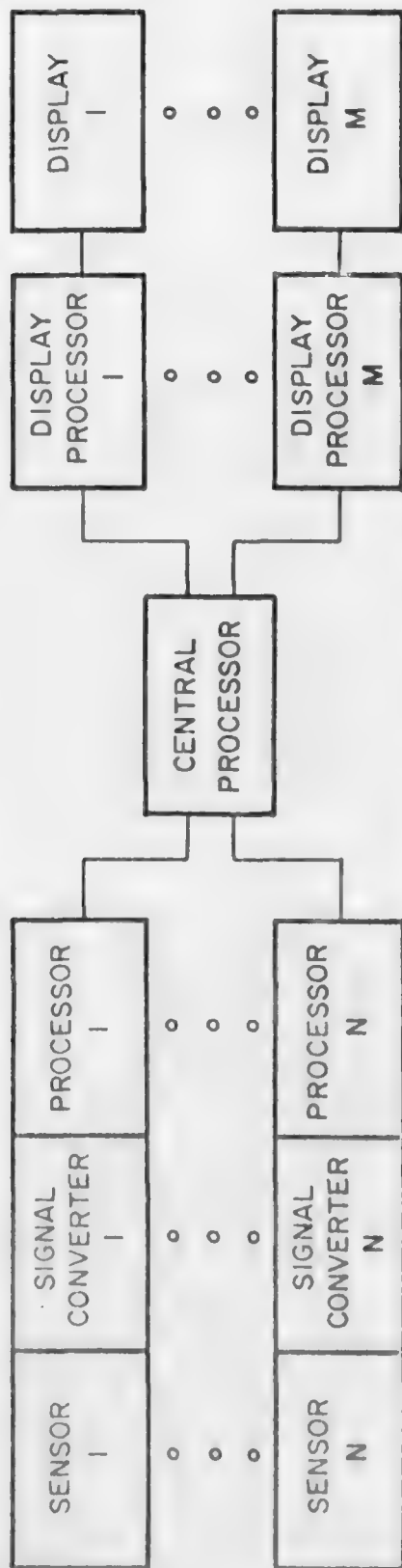
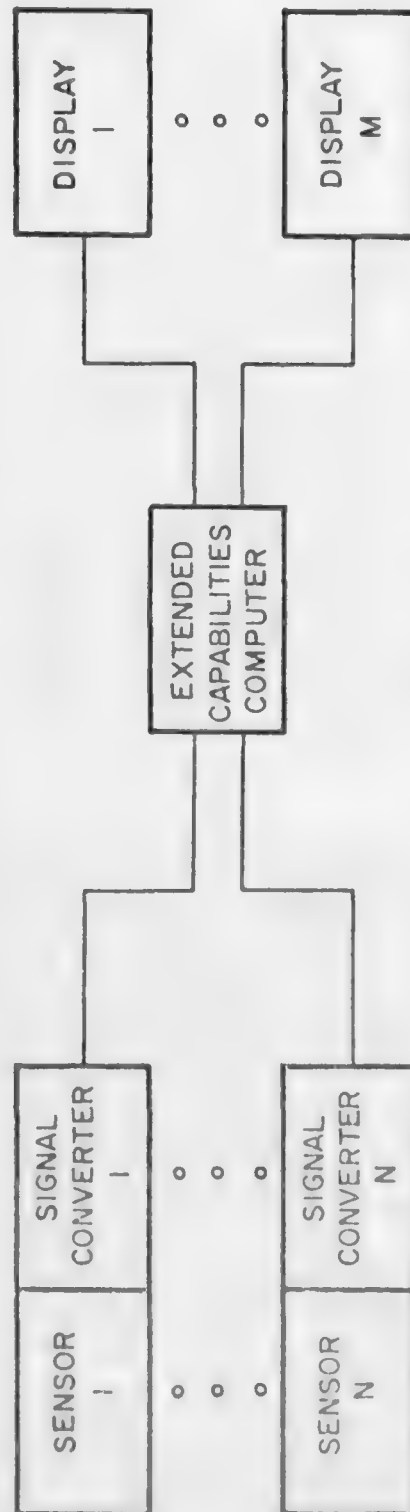


FIGURE 2(a) DISTRIBUTED COMPUTER SYSTEM



CENTRALIZED COMPUTER SYSTEM

Figure 5.2. (continued)

Control Data Corp. Cyber 70 computer that services more than 500 interactive graphics terminals over voice grade telephone lines. In addition to the PLATO IV terminal simulator, other terminal software systems are being developed, including an ASCII Teletype and an IBM 3270. Throughout the design of both the hardware and software of this terminal, an effort has been made to retain maximum flexibility while observing the cost-performance considerations required in the real user environment. Following is a detailed summary of the hardware and software architecture of the intelligent terminal. Also included is a description of some methods of improving the performance of a large scale timesharing system which have been developed using the intelligent terminal on the PLATO IV system.

5.2.1 Hardware Architecture

Figure 5.3 shows the hardware arrangement used in the experimental intelligent terminal. The PDP 11/10 mini-computer is an unmodified 8K core configuration with four "small peripheral controller slots" available. The small peripheral controller slots were used to house the various terminal subsystem interfaces, a ROM bootstrap, the display interface, the communications interface, and the external equipment interface.

The display used in the terminal is a modified Digivue 512-60 display memory unit. Although the display format is similar to that used in the standard PLATO terminal, this unit has been upgraded to operate at character writing rates of up to 6000 characters per second by means of a parallel writing technique [31]. This feature is realized by modifying the display address circuitry.

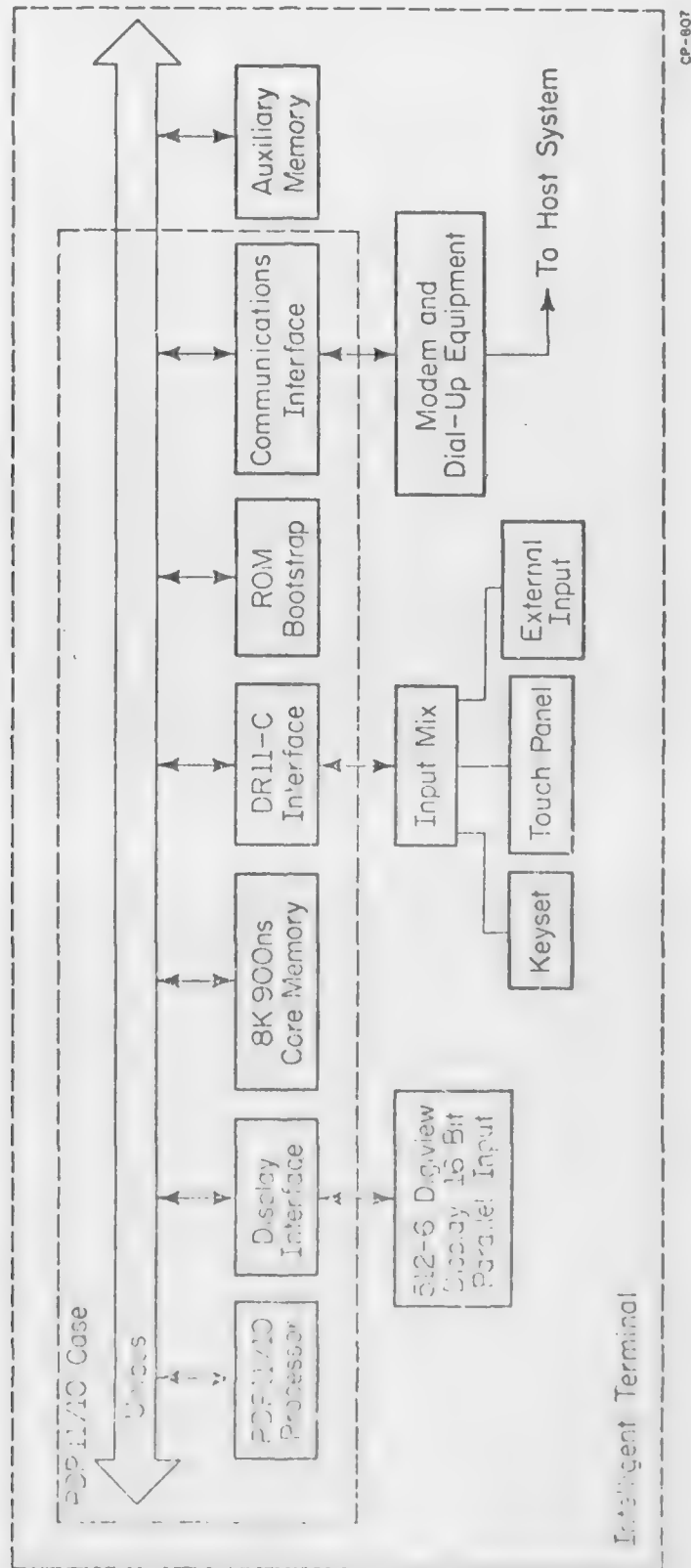


Figure 5.3. Hardware arrangement used in experimental intelligent terminal.

AD-A032 186

ILLINOIS UNIV AT URBANA-CHAMPAIGN COORDINATED SCIENCE LAB F/8 9/2
RESEARCH ON DISPLAY DATA INTEGRATION IN SYSTEMS WHICH USE FLAT --ETC(U)
FEB 75 R L JOHNSON, H G SLOTON, L F WEBER N00014-67-A-0305-0021

UNCLASSIFIED

NL

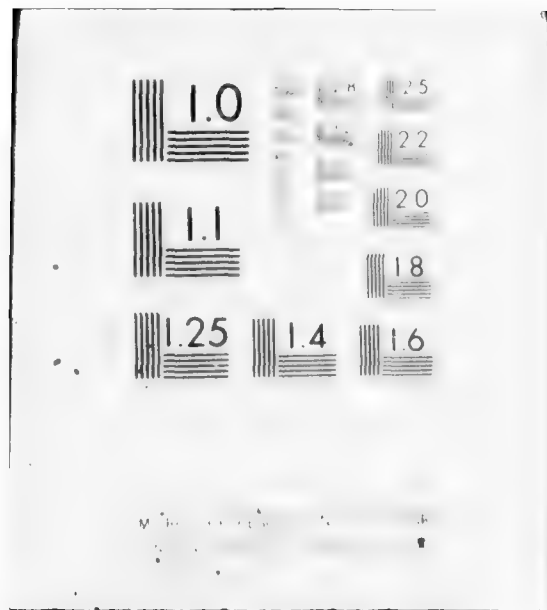
2 of 2

AD
A032-86

END

DATE
FILMED

1 - 77



The present communications interface accommodates PLATO input/output format (20 bit words in; 10 bit words out) and ASCII/EIARS232 signals via program control. Work is presently in progress to allow the format of the communications interface signals to be modified under program control in order to provide automatic access to systems which require different protocols. This approach, while it is somewhat similar to the DEC DL11E communications interface, has an expanded maximum word size to provide for added format variability.

The external equipment interface, the DR11-C, supports user input devices such as keysets of various types, touch input systems, and in later versions, manual manipulation techniques such as light pens, joy sticks, etc. The external equipment interface is also available for use as an input/output port for user controlled devices such as laboratory equipment, educational aids, and office equipment.

As the library of terminal software grows and as additional features of the intelligent terminal (such as expanded character sets and voice input) are implemented, auxiliary forms of low cost storage will be needed. For example, to facilitate a rather sophisticated bootstrap procedure, a 256, 16 bit word ROM has been added to the terminal. It is expected that as character sets, conversion tables, and various loaders are developed, this memory will be expanded. For the larger amounts of auxiliary storage that will be needed, configurations of solid state shift register memory and floppy disk are being evaluated. For example, an 8K MOS shift register memory is being designed and tested that exhibits a worse case access time of 1 μ s and a transfer rate of 1 MHz. An important

aspect of this research is the development of optimum memory hierarchies which will improve the cost-performance characteristics of an intelligent terminal.

5.2.2 Terminal Software

To best accommodate different host systems, the terminal software is arranged as a single resident terminal monitor, with a number of host dependent, and user dependent tasks as shown in Figure 5.4. The combination of the monitor and a host dependent task comprise the nucleus of the terminal simulator for each particular host. All other routines are defined as user dependent tasks. Currently, the intelligent terminal is capable of two modes of operation: as a PLATO IV student terminal, and as an ASCII teletype. Other configurations under consideration are: a graphics terminal compatible with the ARPANET graphics protocol, an IBM 3272 for access to information and retrieval systems, and an extended stand-alone mode such as single user BASIC with added graphics features.

The terminal monitor contains all the software drivers for the plasma panel, including the character generator, a local mode keyset handler with some single line editing capabilities, the file handling system, and all user information. It is capable of a limited stand-alone mode of operation and serves as a transfer point from one mode of operation to another. A user may "escape" to the monitor at any time while using the intelligent terminal. A new host dependent task can then be called, and the intelligent terminal will automatically switch to the new mode, establishing communication with a different host system if necessary. Most

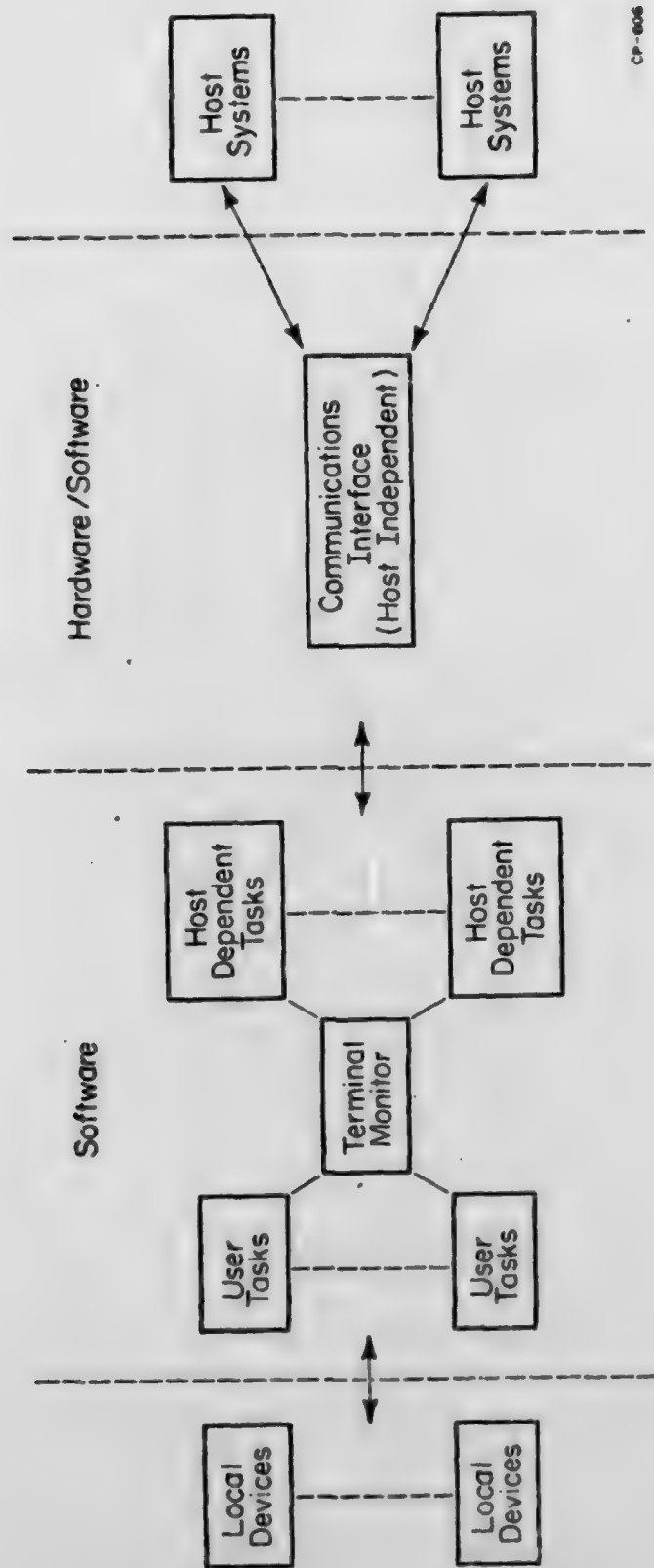


Figure 5.4. Terminal software architecture.

terminal monitor subroutines may also be used by either host dependent or user dependent tasks.

Each host dependent task must interpret data from the communications interface such that the information is either used to call subroutines resident in the terminal monitor, passed to user dependent subroutines, or used within the host dependent task. It may handle all the user input devices directly, or through the monitor subroutines. For most applications, only one host dependent task need be resident. However, if inter-host communication is desired, the tasks for each host must be available. It should be noted that while the possibility of attaching several displays and input devices so as to allow several users to work simultaneously through one mini-processor exists, this problem has not been studied in this project to date.

The most developed host dependent task is the PLATO IV terminal simulator. This task contains all the features described by Stifle [30], plus several new features such as fast area erasure or "block erase", and the facilities for communication between TUTOR [32] programs and terminal resident assembly language subroutines.

Another mode of operation which is now available is the simulation of an ASCII teletype with display. This has been used to communicate with a Burroughs 6700, and a DEC System 10. Inter-host communication has been achieved by formatting information on the PLATO IV system and sending it to the B6700 for extended processing. Plans have been made to communicate with other large scale information and retrieval systems through the

intelligent terminal, and to send the selected information to the PLATO IV system to be displayed as part of information presented as lesson material.

User dependent tasks are those which provide additional features to the basic terminal structure. These include terminal resident sub-routines which communicate with programs executing on the host system, such as those which enhance graphics, and software drivers that control special peripheral equipment. The mini-computer can be configured as a process control machine, yet simultaneously retain the capability of accepting input and transmitting data as a graphics terminal. Since most of the initial work on this terminal has been on the PLATO IV system, nearly all the user dependent tasks now working address themselves to the problems of a large scale timesharing system with a relatively low bandwidth between the central processor and the terminals. Some of these tasks are described later in this paper.

5.3 Specific Studies Relating to the PLATO IV System

Throughout the development of the experimental terminal system, studying the relationship between the host computer and the intelligent terminal processor has been an important aspect of the research. For example, rather than develop a local operating system on the PDP 11/10, the facilities of the host system were used whenever possible. A cross assembler for the PDP11 assembler language (PAL) has been written in TUTOR [32] the educational language for PLATO. This cross assembler runs as a normal TUTOR lesson. The binary output of this assembler is saved on disk in the host system. These binaries can then be inspected, linked, and

sent to the terminal simulator from another TUTOR lesson. A protocol has been established so the user may "log-in" any binary which is loaded in this manner, identifying it by a six character name. The resident program can then be called by name from a TUTOR program. Source code for assembly is stored in the same manner as TUTOR source code, so that all of the PLATO editing and filing systems are available for use.

Another consideration was the bootstrapping procedure. A method was desired that did not require any additional peripherals; so again the host system facilities have been used. A ROM-held bootstrap program sends a signal to PLATO indicating that the terminal is ready to be initialized. PLATO then responds by sending the absolute loader in bootstrap format, and then the monitor and PLATO IV terminal simulator in absolute loader format. Control is passed from the bootstrap to the loader to the monitor without user intervention. Once the monitor is running, the user can request which type of terminal is desired. The appropriate host dependent task is loaded and control is automatically transferred to that task. Currently, all files are kept on the PLATO system. However similar methods of bootstrapping from other host systems or from local storage could be devised.

Another basic problem of using a system based on a large, centrally located computer is the bandwidth limitations of the voice grade communication lines which form the connection between the processing power and the graphic displays. A relatively small amount of local processing capability can effectively increase the bandwidth in several ways. For example, it is a well-known fact that the frequency of occurrence of

symbols and words in a language can be determined, and that this relationship is mostly independent of context. This relation can be used to enhance the performance of a terminal even in a fixed bandwidth system by using more efficient coding schemes. The use of more efficient codes has been generally avoided in terminals because of the increased cost and complexity. With the development of low-cost micro- and mini-processors and memory, use of more efficient codes seems possible with little increase in cost. An investigation of this concept has been initiated using the intelligent terminal system.

Another use of a resident processor is local curve generation. Circles and other conic sections have been produced with significant improvement in generation speed. In addition, the extensive use of the programmable characters to create multicharacter pictures has prompted the following work. In any picture of more than two characters, or roughly $3/4" \times 3/4"$, the individual characters are plotted so slowly as to be noticeable. This problem can be alleviated by sending encoded information to the intelligent terminal and allowing the mini-processor to plot the entire figure at the speed of the parallel panel. A large, block alphabetic character set, each character of which is made up of two to six programmable characters, can now be written at the same speed as the 8×16 dot characters. This is an increase of greater than six times normally available speeds, since extra positioning information must normally be sent with the characters.

5.4 Conclusions of System Studies

The recent advances in micro-processor, memory, and display technology suggest that intelligent terminal architectures, which exhibit interactive, graphic capability and multi-host compatibility, will become economically viable to users of the emerging computer-based information system services. The work described in this paper has dealt with the development of an experimental facility which can be used to model and test both intelligent terminal architecture concepts and terminal hardware techniques. This facility has already been used to develop and demonstrate numerous terminal improvements and host/terminal software concepts. These include more efficient use of the communication bandwidth between the terminal and the host; automatic or programmed controlled access to a variety of host systems which require different communication protocol; and improved task performance as a result of coordination between a centrally located large scale host system and a local mini-computer-based terminal system.

REFERENCES

1. H. Veron and C. C. Wang, "AC Electrical Breakdown of Neon with External Electrodes," J. Appl. Phys., Vol. 43, pp. 2664 (1972).
2. F. M. Lay and C. K. Chu, "Simulation of a Transient DC Breakdown in a Penning Mixture Between Two Closely Spaced Parallel Electrodes," J. Appl. Phys., Vol. 44, p. 4008 (1973).
3. F. M. Lay, C. K. Chu, and P. H. Haberland, "Simulation of Cyclic Operation of Gap Panel Device," IBM J. Res. Develop. Vol. 18, p. 244 (1974).
4. C. Lanza, "A One-Dimensional Numerical Analysis for an AC Gas Display Panel," IBM J. Res. Develop. Vol. 18, p. 232 (1974).
5. A. L. Ward, "Calculations of Cathode-Fall Characteristics," J. Appl. Phys., Vol. 33, p. 2789 (1962).
6. A. L. Ward, "Effect of Space Charge in Cold Cathode Gas Discharge," Physical Review, Vol. 112, No. 6, pp. 1852-1857, December 1958.
7. A. L. Ward, "Effect of Space Charge Upon the Transport of Charged Carriers," J. Appl. Phys., Vol. 35, No. 3, part 1, pp. 469-474, March 1964.
8. A. L. Ward, "Ionization, Diffusion, and Drift Velocities in a Pulsed Townsend Discharge," J. Appl. Phys., Vol. 36, No. 4, pp. 1291-1294, April 1965.
9. W. Börsch-Supan and H. Oser, "Numerical Computation of the Temporal Development of Currents in a Gas Discharge Tube," J. of Research of NBS, Vol. 67B, No. 1, pp. 41-63, January 1963.
10. J. M. Anderson, "Electrodeless Discharge Modes in Neon-Nitrogen Mixture with Application to the Plasma Display Panel," Appl. Phys. Letters, Vol. 16, p. 531 (1970).
11. W. B. Johnson, "Laser Interferometry and Photon Scattering in Plasma Diagnostics," IEEE Transactions on Antennas and Propagation, Vol. AP-15, No. 1, pp. 152-162, January 1967.
12. H. Joseph Hoehn and Richard A. Martel, "Recent Developments in Three-Color Plasma Display Panels," IEEE Transactions on Electron Devices, Vol. ED-20, No. 11, pp. 1078-1081, November 1973.

13. C. Cuthbertson and M. Cuthbertson, "The Refraction and Dispersion of Argon, and Redetermination of the Dispersion of Helium, Neon, Krypton, and Xenon," Proc. of Royal Society of London, Vol. A 84, p. 13 (1910).
14. C. Cuthbertson and M. Cuthbertson, "The Refraction and Dispersion of Neon and Helium," Proc. of Royal Society of London, Vol. A 135, pp. 40-47 (1932).
15. J. T. Verdeyen, B. E. Cherrington, and M. E. Fein, "Spatially Resolved Laser Heterodyne Measurements of Plasma Densities in Weakly Ionized Gases," Applied Physics Letters, Vol. 9, No. 10, pp. 360-362, November 1966.
16. R. H. Wilson, "A Capacitively Coupled Bistable Gas Discharge Cell for Computer Controlled Displays," Report R-303, Coordinated Science Laboratory, University of Illinois, Urbana, Illinois, June 1966.
17. B. M. Arora, "The Influence of Gas Composition and of Signal Waveforms on the Properties of the Plasma Display," Report R-377, Coordinated Science Laboratory, University of Illinois, Urbana, Illinois, May 1968.
18. F. M. Lay, "Relative Photoelectric Yields of Some Metal Films and Dielectrics in an Insulated Electrode Discharge," J. Vac. Sci. Technol., Vol. 11, No. 3, pp. 605-609, May/June 1974.
19. J. D. Schermerhorn, "Internal Random Access Address Decoding in an AC Plasma Display Panel," Digest of Papers, 1974 SID International Symposium, p. 22.
20. S. Umeda and T. Hirose, "Self Shift Plasma Display," Dig. Papers Symp. Soc. Inform. Display, 1972, p. 38.
21. G. S. Weikart, "Independent Subsection Shift and a New Simplified Write Technique for Self Shift AC Plasma Panels," IEEE, SID, AGED 1974 Conference on Display Devices and Systems, New York, 1974.
22. W. D. Petty, "Multiple States and Variable Intensity in the Plasma Panel," Report R-497, Coordinated Science Laboratory, University of Illinois, November 1970.
23. M. DeJule and G. Chodil, "A Gray Scale Technique for a Plasma Panel Display and Similar On-Off Devices," SID Symposium, Digest of Papers, May 1971, pp. 102-103.
24. S. Umeda, et al., "Picture Display with Gray Scale in the Plasma Panel," SID Symposium, Digest of Papers, May 1973, pp. 70-71.
25. K. Kurahashi, et al., "Plasma Display with Gray Scale," SID Symposium, Digest of Papers, May 1973, pp. 72-73.

26. C. N. Judice, et al., "Bi Level Rendition of Continuous Tone Pictures on an AC Plasma Panel," IEEE, SID, AGED 1974 Conference on Display Devices and Systems, New York, 1974.
27. J. O. Limb, "Design of Dither Waveforms for Quantized Visual Signal," BSJT, 68, 1969, pp. 2555-2582.
28. T. S. Huang, "Coding of Graphical Data," Picture Bandwidth Compression, New York, 1972, pp. 233-265.
29. A. B. White, "Video Imaging on the Plasma Panel," master's thesis, University of Illinois, 1975.
30. J. Stifle, "The PLATO IV Student Terminal," University of Illinois, CERL Report X-15, 1973.
31. D. E. Liddle, "A Parallel Addressed, Multiplexed Driver Plasma Display," Digest of Technical Papers, SID International Symposium 1972.
32. J. Ghesquiere, et al., "Introduction to Tutor," Computer-based Education Research Laboratory, University of Illinois, 1974.

REPORT DOCUMENTATION PAGE		READ INSTRUCTIONS BEFORE COMPLETING FORM
1. REPORT NUMBER	2. GOVT ACCESSION NO.	3. RECIPIENT'S CATALOG NUMBER
4. TITLE (and Subtitle) RESEARCH ON DISPLAY DATA INTEGRATION IN SYSTEMS WHICH USE FLAT AC PLASMA PANEL DISPLAYS WITH INHERENT MEMORY.		5. TYPE OF REPORT & PERIOD COVERED Final Technical Report
7. AUTHOR(s) R. L. Johnson (Principal Investigator)		6. PERFORMING ORG. REPORT NUMBER 100-31 Dec 74 CONTRACT OR GRANT NUMBER(s) 15 N00014-67-A-0305-0021 NEW
9. PERFORMING ORGANIZATION NAME AND ADDRESS Coordinated Science Laboratory University of Illinois at Urbana-Champaign Urbana, Illinois 61801		10. PROGRAM ELEMENT, PROJECT, TASK AREA & WORK UNIT NUMBERS
11. CONTROLLING OFFICE NAME AND ADDRESS Office of Naval Research		12. REPORT DATE Feb 1975 13. NUMBER OF PAGES 102
14. MONITORING AGENCY NAME & ADDRESS (if different from Controlling Office) 12 109 F.		15. SECURITY CLASS. (of this report)
16. DISTRIBUTION STATEMENT (of this Report) Approved for public release; distribution unlimited 10 R.L. / Johnson, H.G. / Slottow, L.F. / Weber A.B. / White		
17. DISTRIBUTION STATEMENT (of the abstract entered in Block 20, if different from Report)		
18. SUPPLEMENTARY NOTES		
19. KEY WORDS (Continue on reverse side if necessary and identify by block number) Plasma Display Panels Inherent Memory Spatial Gray Scale		
20. ABSTRACT (Continue on reverse side if necessary and identify by block number) A program of research to explore new display device techniques and digital system architecture concepts which can be used to realize highly reliable low cost interactive graphic display systems has been completed at the University of Illinois Coordinated Science Laboratory. The techniques and concepts which were studied are generally applicable to future large scale computer-based information systems such as those used in ground based operations as well as in specialized computer-based information systems such as those used in aircraft, submarine, and shipboard instrumentation.		

097400

1/R

SECURITY CLASSIFICATION OF THIS PAGE(When Data Entered)

[The main body of the page contains extremely faint, illegible text, likely bleed-through from the reverse side. The text is organized into several paragraphs, but the specific content cannot be discerned.]

SECURITY CLASSIFICATION OF THIS PAGE(When Data Entered)

DISTRIBUTION LIST

Office of Naval Research
Vehicle Warfare Technology
Arlington, Virginia 22217

ATTN: Codes 211

455

430

(4 cys)

(1 cy)

(1 cy)

Defense Documentation Center
Cameron Station

Alexandria, Virginia 23314

(12 cys)

Director

Naval Research Laboratory

Washington, D. C. 20390

ATTN: Tech Info Division

Library, Code 2039

(1 cy)

(1 cy)

Director

Office of Naval Research Branch Office

1000 East Green Street

Palmdena, California 91101

(1 cy)

Office of Naval Research Branch Office

19 Summer Street

Boston, Massachusetts 02210

(1 cy)

Director

Office of Naval Research Branch Office

635 Clark Street

Chicago, Illinois 60605

(1 cy)

Headquarters

Department of the Navy

Naval Material Command

Washington, DC 20360

ATTN: MAT 034

(1 cy)

Commander

Naval Air Systems Command

Washington, DC 20360

ATTN: AIR 53372E

5313A1

340

360

(1 cy)

(1 cy)

(1 cy)

(1 cy)

Commander

Naval Sea Systems Command

Code 09G3

Washington, DC 20360

(1 cy)

Commanding Officer

U. S. Naval Air

Development Center

Warminster, PA 18974

ATTN: Code 402

(1 cy)

Naval Electronics Laboratory Center

271 Catalina Boulevard

San Diego, California 92152

(1 cy)

Commandant, U. S. Marine Corps

Headquarters, U. S. Marine Corps

Washington, DC 20591

ATTN: RD-1

(1 cy)

Commandant

U. S. Coast Guard Headquarters

400 7th Street, NW

Washington, DC 20591

(1 cy)

Commanding General

U. S. Army Material Command

Washington, DC 20315

ATTN: AMCRD-HA (C. Robinson)

(1 cy)

E-A Industrial Corporation

4500 N. Shallowford Road

Chamblee, Georgia 30341

ATTN: R. J. Jelley

(1 cy)

Director

Human Engineering Labs

Aberdeen Proving Grounds, MD

ATTN: AMXRD-HEL (J. Barnes)

(1 cy)

U. S. Air Force

Office of Scientific Research

AFOSR (NL)

1400 Wilson Boulevard

Arlington, Virginia 22207

(1 cy)

Aero Medical Research Laboratory

(MRHD)

Wright Patterson AFB, Ohio 45433(1 cy)

Headquarters AFSC-XRLA

Andrews AFB 20334

ATTN: LT COL Dander

(1 cy)

Commander
Air Force Avionics Laboratory
Wright-Patterson AFB, Ohio 45433
ATTN: AFAL/AMM (1 cy)

Magnavox Co.
100 Magnavox Way
FL. Wayne, Indiana 46804
ATTN: Tom Holloway (1 cy)

New Mexico State University
P. O. Box 5095
Las Cruces, New Mexico 88001
ATTN: Dr. W. H. Teichner (1 cy)

Martin-Marietta Corporation
Orlando Division
Post Office Box 5837
Orlando, Florida 32805
ATTN: Dr. D. B. Jones (1 cy)

Virginia Polytechnic Institute
Dept. of Industrial Engineering
Blacksburg, Virginia 24061
ATTN: Dr. H. L. Snyder (1 cy)

Honeywell, Inc.
Systems and Research Division
200 Ridgway Parkway
Minneapolis, Minnesota 55413 (1 cy)

